REPORT DOCUMENTATION PAGE

Form Approved OMB NO. 0704-0188

The public reporting burden for this collection of information is estimated to average 1 hour per response, including the time for reviewing instructions, searching existing data sources, gathering and maintaining the data needed, and completing and reviewing the collection of information. Send comments regarding this burden estimate or any other aspect of this collection of information, including suggesstions for reducing this burden, to Washington Headquarters Services, Directorate for Information Operations and Reports, 1215 Jefferson Davis Highway, Suite 1204, Arlington VA, 22202-4302. Respondents should be aware that notwithstanding any other provision of law, no person shall be subject to any oenalty for failing to comply with a collection of information if it does not display a currently valid OMB control number.
PLEASE DO NOT RETURN YOUR FORM TO THE ABOVE ADDRESS.

1. REPORT DATE (DD-MM-YYYY)	2. REPORT TYPE	3. DATES COVERED (From - To)
06-08-2014	MS Thesis	-

4. TITLE AND SUBTITLE	5a. CONTRACT NUMBER
Bound electron states in skew-symmetric quantum wire intersections	W911NF-11-1-0189
	5b. GRANT NUMBER
	5c. PROGRAM ELEMENT NUMBER
	206022

6. AUTHORS	5d. PROJECT NUMBER
Liubov Zhemchuzhna (student), Igor Bondarev (advisor)	
	5e. TASK NUMBER
	5f. WORK UNIT NUMBER

7. PERFORMING ORGANIZATION NAMES AND ADDRESSES	8. PERFORMING ORGANIZATION REPORT NUMBER
North Carolina Central University Graduate Office of Sponsored Programs 1801 Fayetteville St. Durham, NC 27707 -3129	

9. SPONSORING/MONITORING AGENCY NAME(S) AND ADDRESS (ES)	10. SPONSOR/MONITOR'S ACRONYM(S)
U.S. Army Research Office P.O. Box 12211 Research Triangle Park, NC 27709-2211	ARO
	11. SPONSOR/MONITOR'S REPORT NUMBER(S)
	58986-PH-REP.29

12. DISTRIBUTION AVAILIBILITY STATEMENT

Approved for public release; distribution is unlimited.

13. SUPPLEMENTARY NOTES

The views, opinions and/or findings contained in this report are those of the author(s) and should not contrued as an official Department of the Army position, policy or decision, unless so designated by other documentation.

14. ABSTRACT

The lowest energy bound state has been analyzed for an electron trapped at the intersection of two identical narrow channels (quantum wires), crossed at an arbitrary angle with the cross-section area in the form of a square. When the channels are perpendicular, such a classically unbound electron system is known to possess a quantum bound (trapped) state. A new improved trial wave function is proposed and used to tackle the problem. The S-type wire intersection preserves the bound state even at angles close to zero degree. These results supplement a theory

15. SUBJECT TERMS

Quantum Wires, Crossed Nanowires, Trapped Electron States, Quantum Dots

16. SECURITY CLASSIFICATION OF:			17. LIMITATION OF ABSTRACT	15. NUMBER OF PAGES	19a. NAME OF RESPONSIBLE PERSON
a. REPORT	b. ABSTRACT	c. THIS PAGE			Igor Bondarev
UU	UU	UU	UU		19b. TELEPHONE NUMBER
					919-530-6623

Standard Form 298 (Rev 8/98)
Prescribed by ANSI Std. Z39.18

Report Title

Bound electron states in skew-symmetric quantum wire intersections

ABSTRACT

The lowest energy bound state has been analyzed for an electron trapped at the intersection of two identical narrow channels (quantum wires), crossed at an arbitrary angle with the cross-section area in the form of a square. When the channels are perpendicular, such a classically unbound electron system is known to possess a quantum bound (trapped) state. A new improved trial wave function is proposed and used to tackle the problem. The S-type wire intersection preserves the bound state even at angles close to zero degree. These results supplement a theory of quantum bound states in classically unbound systems and may be useful to interpret electron transport peculiarities in realistic systems such as semiconductor nanowire films and carbon nanotube bundles.

Bound electron states in skew-symmetric quantum wire intersections

by

Liubov Zhemchuzhna

A Thesis (Project) Submitted to
The Faculty of the Graduate School at
North Carolina Central University
In Partial Fulfillment of the Requirements
For the Degree
Master of Science in Physics

Durham, North Carolina

2014

Approved by:

Committee Chair

Committee co-Chair

Committee co-Chair

ABSTRACT

The lowest energy bound state has been analyzed for an electron trapped at the intersection of two identical narrow channels (quantum wires), crossed at an arbitrary angle with the cross-section area in the form of a square. When the channels are perpendicular, such a classically unbound electron system is known to possess a quantum bound (trapped) state. A new improved trial wave function is proposed and used to tackle the problem. The S-type wire intersection preserves the bound state even at angles close to zero degree. These results supplement a theory of quantum bound states in classically unbound systems and may be useful to interpret electron transport peculiarities in realistic systems such as semiconductor nanowire films and carbon nanotube bundles.

ACKNOWLEDGMENTS

I want to express my total, utter gratitude to my advisor, **Professor I. V. Bondarev** for his charitable help and support throughout the whole course of my studies, including this thesis preparation as well as general Theoretical Physics courses. Without his assistance and dedicated involvement in every step throughout the process, this thesis would have never been accomplished. I would like to thank you so much for your support and understanding over these past two years.

Special thanks go to **Areg Meliksetyan**, a postdoctoral fellow at North Carolina Central University. I appreciate his very useful comments on the subject, his enthusiasm for the topic made a strong impression on me.

Contents

Chapter 1

Literature review

1.1 Quantum dots, their physical properties and applications

Quantum physics is progressing rapidly. Quantization and spin were discovered through optical studies, as were other fundamental atomic properties. With the advent of the laser, physicists learned how to manipulate atomic wavefunctions by applying coherent optical fields. More discoveries followed. Now, at the beginning of the new century, optical techniques are being used to explore a new scientific frontier: the atom-like entities known as quantum dots.

A quantum dot is a nanocrystal made of semiconductor materials that are small enough to exhibit quantum mechanical properties, as shound in (fig1), semiconductor structures in which the electron wavefunction is confined in all three dimensions by the potential energy barriers that form the quantum dots boundaries [4, 3]. A quantum dots electronic response, like that of a single atom, is manifest in its discrete energy spectrum, which appears when electron-hole pairs are excited. Although the wavefunction of a quantum dot electron, and its corresponding hole, extends over many thousands of lattice atoms, the pair–termed an exciton–behaves in a quantized and coherent fashion.

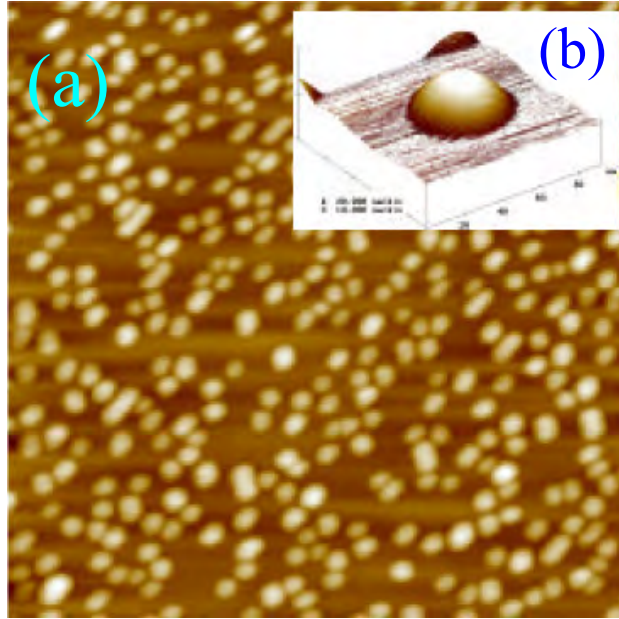The coherence is relatively easy to detect and control optically - for

Figure 1.1: AFM micrographs of: (a) 1 μm x 1 μm surface imaging of $InAs$ quantum dots on $GaAs/InP$, (inset) a single $InAs$ quantum dot.

two reasons. First, the superposition of the ground and excited states dephases more slowly in quantum dots than in higher-dimensional semiconductor structures. Second, quantum dots have large dipole moments (50-100 times larger than those of atoms). Thanks to these advantages, it is possible to probe and manipulate the wavefunction of a single quantum [9].

How can one understand the excited electronic states of a nanometer sized semiconductor crystallite, given that the crystallite structure is simply that of an excised fragment of the bulk lattice? This question is motivated by recent experiments on chemically synthesized "quantum crystallites," sometimes called "quantum dots," in which it is observed that the optical spectra are quite sensitive to size. For example, bulk crystalline CdSe is a semiconductor with an optical bandgap at $690 \, nm$, and continuous optical absorption at shorter wavelengths. However, $3540-$diameter $CdSe$ crystallites containing some 1500 atoms exhibit a series of discrete excited states with a lowest excited state at 530nm (1-3). With increasing size, these states shift red and merge to form the optical absorption of the bulk crystal. Electron microscopy

and BraggX-ray scattering measurements show that these crystallites have the same structure and unit cell as the bulk semiconductor. Such changes have now been observed in the spectra of many different semiconductors.This phenomenon is a "quantum size effect" related to the development of the band structure with increasing crystallite size. Smaller crystallites behave like large molecules (e.g. polycyclic aromatic hydrocarbons) their spectroscopic and photophysical properties. They are true "clusters"that do not exhibit bulk semiconductor electronic properties.

Quantum dots possess another attractive property. Their size, shape, and composition can all be ailored to create a variety of desired properties. These "artificial atoms" can, in turn, be positioned and assembled into complexes that serve as new materials. Many types of quantum dot materials have already been developed. In the early 1980s that papers in the Russian literature, by Ekimov and Efros, gave the first experimental and theoretical description of 3D quantum confinement with semiconductor nanocrystals [10, 11].

There are discovered quantum dots in a glass matrix (they are developed a growth technique of the semiconductor microcrystals in a glassy dielectric matrix. This technique permits to vary the size of the grown microcrystals in a controlled manner from some tens to thousands of angstroms) and in colloidal solutions by Louis E.Brus [12]. The term "quantum dot" was coined by M. Reed.[6] (The approach he used to produce quantum dot nanostructures suitable for electronic transport studies was to confine resonant-tunneling heterostructures laterally with a fabrication-imposed potential. This approach embeds a quasibound quantum dot between two quantum wire contact.) Among them are quantum dots formed by electrostatic gates. Researchers study these quantum dots with far-infrared spectroscopy and with transport techniques, such as conductance measurements. Great advances have been made with electrostatic quantum dots, but this type of quantum dot does not interact strongly with light because the electrostatic gates separate the electrons and holes, severely reducing the quantum dots dipole moment.

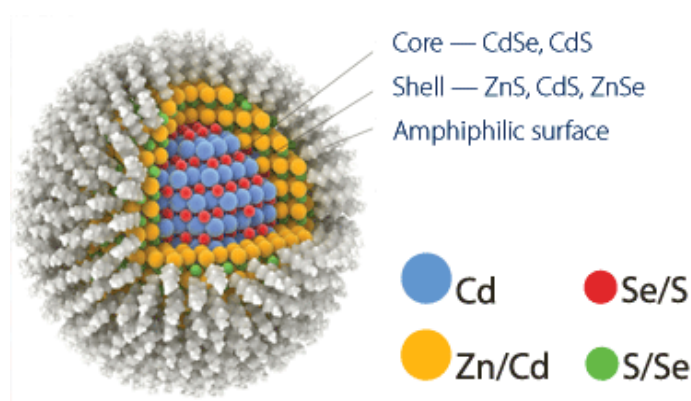Fortunately, some types of quantum dots do interact strongly with light

Figure 1.2: Colloidal quantum dots general schematic

and are being studied in detail, even at the single quantum dot level. Grown as part of a larger crystalline structure,epitaxial quantum dots form spontaneously in molecular beam epitaxy [13]. Epitaxial quantum dots are especially attractive to researchers because they lack the defects caused by etching, regrowth, and other processing steps. Another advantage of epitaxial quantum dots is that they lie far beneath the surface of the surrounding material whose associated states are potentially meddlesome. Colloidal chemistry provides yet another way of growing quantum dots.

Colloidal quantum dots - semiconductor nanocrystals with a size in the range 10 - 20 nm consisting of 10^3-10^5 atoms that are based on inorganic semiconductor materials, covered with a monolayer of the stabilizer ("coat" of organic molecules). Colloidal quantum dots combined physical and chemical properties of molecules with optoelectronic properties of semiconductors (fig2).

Colloidal semiconductor nanocrystals are synthesized from precursor compounds dissolved in solutions, much like traditional chemical processes. The synthesis of colloidal quantum dots is done by using precursors, organic surfactants, and solvents. Heating the solution at high temperature, the precursors decompose forming monomers which then nucleate and generate nanocrystals. The temperature during the synthetic process is a critical factor in determining optimal conditions for the nanocrystal growth. It must be high enough to allow for rearrangement and annealing of atoms during

the synthesis process while being low enough to promote crystal growth. The concentration of monomers is another critical factor that has to be stringently controlled during nanocrystal growth. The growth process of nanocrystals can occur in two different regimes, "focusing" and "defocusing". At high monomer concentrations, the critical size (the size where nanocrystals neither grow nor shrink) is relatively small, resulting in growth of nearly all particles. In this regime, smaller particles grow faster than large ones (since larger crystals need more atoms to grow than small crystals) resulting in "focusing" of the size distribution to yield nearly mono-disperse particles. The size focusing is optimal when the monomer concentration is kept such that the average nanocrystal size present is always slightly larger than the critical size. Over time, the monomer concentration diminishes, the critical size becomes larger than the average size present, and the distribution "defocuses".

There are colloidal methods to produce many different semiconductors. Typical dots are made of binary alloys such as cadmium selenide, cadmium sulfide, indium arsenide, and indium phosphide. Dots may also be made from ternary alloys such as cadmium selenide sulfide. These quantum dots can contain as few as 100 to 100,000 atoms within the quantum dot volume, with a diameter of 10 to 50 atoms. This corresponds to about 2 - 10 nm, and at 10 nm in diameter, nearly 3 million quantum dots could be lined up end to end and fit within the width of a human thumb.

Large batches of quantum dots may be synthesized via colloidal synthesis. Due to this scalability and the convenience of benchtop conditions, colloidal synthetic methods are promising for commercial applications. It is acknowledged to be the least toxic of all the different forms of synthesis.

In a semiconductor crystallite whose diameter is smaller than the size of its exciton Bohr radius, the excitons are squeezed, leading to quantum confinement. The energy levels can then be modeled using the particle in a box model in which the energy of different states is dependent on the length of the box. Quantum dots are said to be in the *weak confinement regime* if their radii are on the order of the exciton Bohr radius; quantum dots are said to be in the 'strong confinement regime' if their radii are smaller than
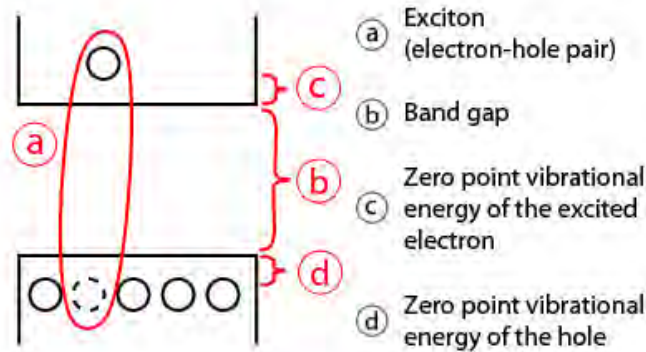
Figure 1.3: Exciton energy levels

the exciton Bohr radius. If the size of the quantum dot is small enough that the quantum confinement effects dominate (typically less than $10nm$), the electronic and optical properties are highly tunable (fig4) [reference]. Fluorescence occurs when an excited electron relaxes to the ground state and combines with the hole. In a simplified model, the energy of the emitted photon can be understood as the sum of the band gap energy between the occupied level and the unoccupied energy level, the confinement energies of the hole and the excited electron, and the bound energy of the exciton (the electron-hole pair).

The band gap can become larger in the strong confinement regime where the size of the quantum dot is smaller than the Exciton Bohr radius a_{b*} as the energy levels split up. where $a_{b*}$is the Bohr radius $r_B = 0.053\,nm$, m is the mass.This results in the increase in the total emission energy (the sum of the energy levels in the smaller band gaps in the strong confinement regime is larger than the energy levels in the band gaps of the original levels in the weak confinement regime) and the emission at various wavelengths; which is precisely what happens in the sun, where the quantum confinement effects are completely dominant and the energy levels split up to the degree that the energy spectrum is almost continuous, thus emitting white light.

The exciton entity can be modeled using the particle in the box. The electron and the hole can be seen as hydrogen in the Bohr model with the
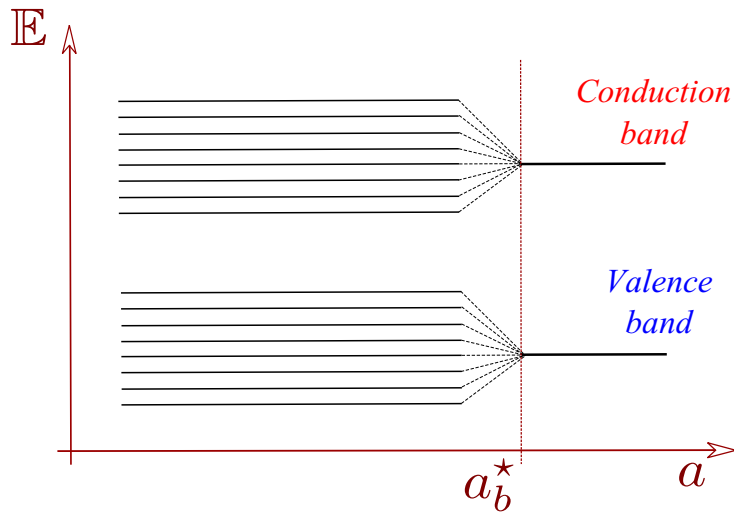
Figure 1.4: Splitting of energy levels for small quantum dots due to the quantum confinement effect. The horizontal axis is the radius, or the size, of the quantum dots and a_{b*} is the Exciton Bohr radius.

hydrogen nucleus replaced by the hole of positive charge and negative electron mass. Then the energy levels of the exciton can be represented as the solution to the particle in a box at the ground level (n = 1) with the mass replaced by the reduced mass. Thus by varying the size of the quantum dot, the confinement energy of the exciton can be controlled. There is Coulomb attraction between the negatively charged electron and the positively charged hole. The negative energy involved in the attraction is proportional to Rydberg's energy and inversely proportional to square of the size-dependent dielectric constant [15] of the semiconductor. When the size of the semiconductor crystal is smaller than the Exciton Bohr radius, the Coulomb interaction must be modified to fit the situation.

Although the above equations were derived using simplifying assumptions, the implications are clear; the energy of the quantum dots is dependent on their size due to the quantum confinement effects, which dominate below the critical size leading to changes in the optical properties. This effect of quantum confinement on the quantum dots has been experimentally verified [16] and is a key feature of many emerging electronic structures [17]. Besides confinement in all three dimensions (i.e., a quantum dot), other quantum con-

Figure 1.5: Colloidal quantum dots general schematics.

fined semiconductors include:Quantum wires, which confine electrons or holes
in two spatial dimensions and allow free propagation in the third.Quantum
wells, which confine electrons or holes in one dimension and allow free prop-
agation in two dimensions.

Quantum size effects play a key role in the optoelectronic properties of
quantum dots. The energy spectrum of the quantum dot is fundamentally
different from the bulk semiconductor . Electron in a nanocrystal behaves
like a three -dimensional potential well. There are several stationary energy
levels for electron and a hole with a characteristic distance between them.
The energy spectrum of the quantum dot depends on its size . Similarly,
the transition between the transition energy in the atom , the transition of
charge carriers between the energy levels in the quantum dot can be emitted
or absorbed photon. Transition frequencies , i.e long wave absorption or
luminescence easily manage changing the dimensions of the quantum dots.
Therefore, quantum dots are sometimes called "artificial points ." In terms of
semiconductor materials that can be called the ability to control the effective
band gap.

There is another fundamental property distinguishing colloidal quantum
dots of semiconductor materials - the possible existence in the form of solu-
tions. (Fig.5). Synthesis of colloidal quantum dots is wide as possible to ob-
tain the quantum dots on the basis of various semiconductors and the prepa-
ration of quantum dots with different geometry (shape). Colloidal quantum

dots are characterized by: the composition, size and shape. Exsist many forms of quantum dots spherical, ellipsoidal, nanocrystals with complex geometry, multi-quantum dots [9].

The various types of quantum dots each have their advantages and disadvantages and allhave served as useful models in research aimed at gaining a better understanding of theoretical properties of quantum dots.

Researchers have studied applications for quantum dots in transistors, solar cells, LEDs, and diode lasers. They have also investigated quantum dots as agents for medical imaging and as possible qubits in quantum computing. The first commercial release of a product utilizing quantum dots was the Sony XBR X900A series of flat panel televisions released in 2013.

Quantum dots are particularly significant for optical applications due to their high extinction coefficient. In electronic applications they have been proven to operate like a single electron transistor and show the Coulomb blockade effect. Quantum dots have also been suggested as implementations of qubits for quantum information processing.

The ability to tune the size of quantum dots is advantageous for many applications. For instance, larger quantum dots have a greater spectrum-shift towards red compared to smaller dots, and exhibit less pronounced quantum properties. Conversely, the smaller particles allow one to take advantage of more subtle quantum effects.

Being zero-dimensional, quantum dots have a sharper density of states than higher-dimensional structures. As a result, they have superior transport and optical properties, and are being researched for use in diode lasers, amplifiers, and biological sensors. Quantum dots may be excited within a locally enhanced electromagnetic field produced by gold nanoparticles, which can then be observed from the surface plasmon resonance in the photoluminescent excitation spectrum of $(CdSe)$ ZnS nanocrystals. High-quality quantum dots are well suited for optical encoding and multiplexing applications due to their broad excitation profiles and narrow/symmetric emission spectra. The new generations of quantum dots have far-reaching potential for the study of intracellular processes at the single-molecule level, high-resolution cellular imaging, long-term in vivo observation of cell trafficking,

tumor targeting, and diagnostics.

Quantum dot technology is one of the most promising candidates for use in solid-state quantum computation. By applying small voltages to the leads, the flow of electrons through the quantum dot can be controlled and thereby precise measurements of the spin and other properties therein can be made. With several entangled quantum dots, or qubits, plus a way of performing operations, quantum calculations and the computers that would perform them might be possible.

Quantum dots may be able to increase the efficiency and reduce the cost of today's typical silicon photovoltaic cells. According to an experimental proof from 2004, quantum dots of lead selenide can produce more than one exciton from one high energy photon via the process of carrier multiplication or multiple exciton generation (MEG). This compares favorably to today's photovoltaic cells which can only manage one exciton per high-energy photon, with high kinetic energy carriers losing their energy as heat. Quantum dot photovoltaics would theoretically be cheaper to manufacture, as they can be made "using simple chemical reactions."

There are several inquiries into using quantum dots as light-emitting diodes to make displays and other light sources, such as "QD-LED" displays, and "QD-WLED" (White LED). In June 2006, QD Vision announced technical success in making a proof-of-concept quantum dot display and show a bright emission in the visible and near infra-red region of the spectrum. Quantum dots are valued for displays, because they emit light in very specific gaussian distributions. This can result in a display that more accurately renders the colors that the human eye can perceive. Quantum dots also require very little power since they are not color filtered. Additionally, since the discovery of "white-light emitting" QD, general solid-state lighting applications appear closer than ever. A color liquid crystal display (LCD), for example, is usually backlit by fluorescent lamps (CCFLs) or conventional white LEDs that are color filtered to produce red, green, and blue pixels. A better solution is using a conventional blue-emitting LED as light source and converting part of the emitted light into pure green and red light by the appropriate quantum dots placed in front of the blue LED. This type of white light as

backlight of an LCD panel allows for the best color gamut at lower cost than a RGB LED combination using three LEDs.

Quantum dot displays that intrinsically produce monochromatic light can be more efficient, since more of the light produced reaches the eye.QD-LEDs can be fabricated on a silicon substrate, which allows integration of light sources onto silicon-based integrated circuits or microelectromechanical systems. A QD-LED integrated at a scanning microscopy tip was used to demonstrate fluorescence near-field scanning optical microscopy (NSOM) imaging.

Quantum dot photodetectors (QDPs) can be fabricated either via solution-processing, or from conventional single-crystalline semiconductors. Conventional single-crystalline semiconductor QDPs are precluded from integration with flexible organic electronics due to the incompatibility of their growth conditions with the process windows required by organic semiconductors. On the other hand, solution-processed QDPs can be readily integrated with an almost infinite variety of substrates, and also postprocessed atop other integrated circuits. Such colloidal QDPs have potential applications in surveillance, machine vision, industrial inspection, spectroscopy, and fluorescent biomedical imaging.

A variety of theoretical frameworks exist to model optical, electronic, and structural properties of quantum dots. These may be broadly divided into quantum mechanical, semiclassical, and classical.

1.2 Quantum bound states in classically unbound regions

Advances in fine-line lithography allow creation of devices which conduct along two-dimensional surfaces, or quantum wires, with nanoscale width, which allow electrons to propagate in the channels formed by these surfaces, but require the electron wave function to vanish on the boundary of the surface [1, 27]. Quantum wires have been used extensively to investigate quantum interference effects [28, 29, 30, 31, 32, 33]. Quantum-mechanical coherence in disordered metals and the associated interference phenomena are

at the heart of many topics which have generated intense interest, including localization, resonant tunneling, and universal conductance fluctuations [29].
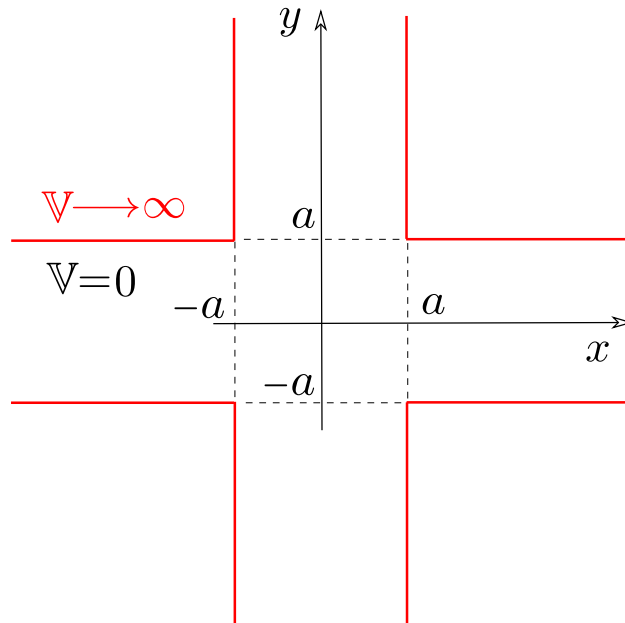

Figure 1.6: Schematic diagram of the potential formed by the crossed wires.

Schult et. al reported in Ref. [1] calculations designed to determine whether an electron can be trapped at the intersection of the perpendicularly aligned quantum wires, due to a quantum effects. The presence of such trapped electrons could modify considerably the operation of devices made of these wires. It should be noted that, as such surfaces have no "classically forbiden" region (a classical particle could roll freely through such a system), the discovery by Schult et. al [1] (and earlier by Lenz et. al [34]) that such systems possess a bound state was rather surprising. It shows the quantum binding of a classically unbound system, and thus complements the phenomenon of the decay of a classically bound stte by quantum tunneling. Goldstone and Jaffe [35, 36] (and Exner [37, 38]) then proved the remarkable result that at least one bound state exists for all two-dimensional surfaces of constant width (except surfaces of constant curvature, which have no bound state).

The authors of [1] asserted that the detailed shape of the potential which

confines the electron to the channel is not important in determining the qualitative fact of the presence of a bound state at the intersection. For an initial wave function which is odd about the x and y center lines and even about the $x = y$ line, the energy is $E_2 = 3.72E_t$. No bound states are found which are od about the $x = y$ line. The main disadvantage of this mesh-point method is, that it gives only the lowest state of each symmetry class. Possible higher-energy bound states would be inaccessible. For these the Authors of Ref. [1] reported their second method which uses an expansion in a complete set of solutions of the differential equation $\Delta\Psi = -k^2\Psi$ (for a trial value of k^2) in each of the five large rectangular regions shown in Fig. (2.1). The coefficients in this expansion should be chosen to match Ψ and its derivatives at the boundaries between these regions. One of the advantages of this method is that it can be extended to energies above the propagation threshold. Also it can be easily extended to any geometry composed of rectangles, open or closed, with equal of different width. For a tight-binding approach to such problems, see [40]. This method may be used to investigate the importance of the sharp corners in forming the bound state, and the amount of bend required to form a bound state of the bent wire.

As is well known (see [41]), a "bulge" in a two-dimensional surface can be mapped into one dimension; the transverse bulge then appears as an effective local attraction, which in one dimension always produces a bound state. However, it was surprising to find that a bend produces an effective attraction similar to a bulge. The existence of these bound states can be understood qualitatively. In Refs. [42, 43] Carini et. al examined the properties of systems containing a single bend. The Authors examined in Ref. [43] bent waveguides which support several bound states. They investigated this question from both theoretical and experimental perspectives, by calculating energies and fields for such states in bent waveguides (such as in Fig. (1.8), constructing such waveguides, and comparing their experimental properties with the theoretical predictions. In [41] Carini et. al examine the case of a system with two right-angle bends as shown in Fig. 1.7. The width of the straight sections is W and the height of the bend is H. First they consider the case where the straight sections of the wire are infinitely long.

The wave function for the electron satisfies the equation

$$(\nabla^2 + k^2)\psi(x, y) = 0, \qquad \psi|_{\mathcal{S}} = 0, \qquad (1.1)$$

where the wave number k is related to the energy E by $k^2 = 2m^*E/\hbar^2$. In either straight section the requirement that the wave function vanish on the boundary, and separability of the Hamiltonian, forces the y dependence of the wave function to be of the form $\sin(n\pi y/W)$ for integer n. This transverse quantization condition produces an energy threshold; the lowest energy allowed for free propagation is $E_{thr} = (\hbar\pi)^2/(2m^*W^2)$. Both the extra space in the bend(s) of the wire, and the bending itself, produce an effective attraction which supports electron bound state(s) in the region of the bend(s). The wire of Fig. 1.7 will have one or two bound states, which appear as isolated states with energy below the threshold energy E_{thr}. The bound state wave functions will be largest in the vicinity of the bend, and fall off exponentially with distance from the bend region.
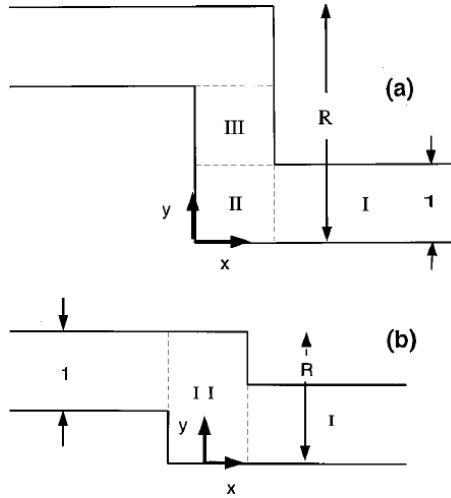

Figure 1.7: (From Ref. [41]) Simplified model for bent quantum wire. Infinitely long wire with two right-angle bends, the width arbitrarily normalized to 1 and the aspect ratio (height/width ratio) R. (a) the aspect ratio $R > 2$ is the "quantum bend discontinuity" case of Ref. [48]. For the purpose of calculations the wire is divided into three sections labeled I, II, and III, respectively. (b) The aspect ratio $1 < R < 2$ is he "quantum bend continuity" case. the wire is divided into sections labeled I and II, respectively.

Thus, bent quantum wires are examples of quantum systems whose bound states do not arise from the "traditional" picture, where a binding potential creates classically allowed and forbidden regions. Here the boundary conditions (vanishing of the wave function on the boundaries of the wire) give rise to transverse quantization conditions which produce a minimum threshold energy for continuum solutions. Localized bends or bulges in these wires then produce effective local attractive forces which give rise to bound states. As the effective attraction in a bent wire is (to lowest order) proportional to the square of the curvature of the wire,[35, 36] the magnitude of the binding energy increases as the curvature increases.

The analogy of bent two-dimensional systems and rectangular waveguides is considered in Refs. [42, 43]. Suppose, one has some two-dimensional curve σ in the xy plane, which possesses a scalar field ψ satisfying the Helmholtz (or Schrödinger) equation $[\nabla^2 + k^2]\psi = 0$, with $\psi|_{\mathcal{S}} = 0$ on the boundary $\mathcal{S}$ of the curve, then one can produce a rectangular waveguide by translating the curve σ normally in the z direction. E and B fields can be constructed from ψ as follows:

$$\mathbf{E}(x,y) = ik\hat{\mathbf{z}}\psi(x,y), \qquad \mathbf{B}(x,y) = -\hat{\mathbf{z}} \times \nabla\psi \qquad (1.2)$$

The E and B fields of this equation will satisfy Maxwell's equations and boundary conditions for TE modes in the waveguide (see e.g. [44]), where the electron wave number k is related to the frequency $f = \omega/2\pi$ by

$$k \rightarrow \frac{2\pi\sqrt{\mu\epsilon}f}{c}. \qquad (1.3)$$

Therefore if there exist bound states of the Schrödinger equation for particles moving in the two-dimensional curve σ (i.e., solutions of the wave equation below the minimum energy for free propagation of waves in the wire), there will be analogous confined TE modes (solutions of E and B fields with frequencies below the cutoff frequency for the waveguide), and the confined $\mathbf{E}$ field of Eq. (1.2) will be described by the same scalar function ψ which constitutes the bound state wave function of the electron in the quantum wire,

in Eq. (1.1)

Having shown correspondence between wave functions for the electrons moving freely in a quantum wire, and the electric field for TE modes in a rectangular waveguide (see also [37, 38, 27, 28, 29, 45, 42]), Carini et. al [41] constructed waveguides of corresponding shape, and demonstrated the location of the confined states by measuring the ratio of reflected to incident power $R(f)$ as a function of frequency f for microwaves. By understanding the properties of the waveguides, one can gain information about the quantum channels or wires. They have shown that theoretical calculations give very good agreement with experiments of confined electromagnetic fields in bent waveguides. They showed that the number of confined electric field modes, and their location, are determined by the geometry of the waveguide.
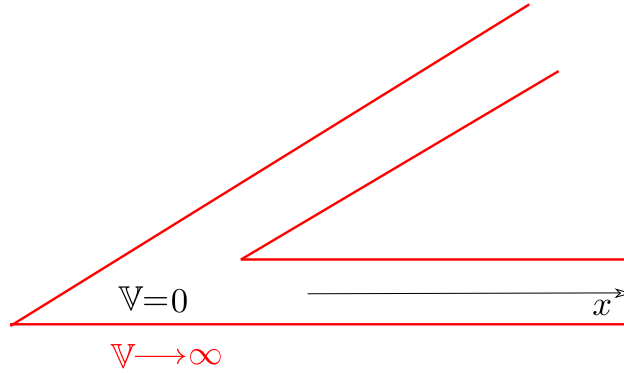

Figure 1.8: Sharply bent two-dimensional surface.

Experimental studies have been carried out for quantum wires with two bends by Wu and collaborators [46, 47]. Wang and collaborators [48] carried out theoretical calculations of the conductance for electrons in this geometry, and compared it to these experimental results.

Obviously, the considered cross-shaped region received application in the field of connected wave guides [21]. Trapped quantum modes in complex three-dimensional systems were addressed in [22]. The eigenstates of an electron in an infinite quantum waveguide (e.g., a bent strip or a twisted tube) are often trapped or localized in a bounded region that prohibits the electron transmission through the waveguide at the corresponding energies. We

revisit this statement for resonators with long but finite branches that is called finite waveguides. Although the Laplace operator in bounded domains has no continuous spectrum and all eigenfunctions have finite L2 norm, the trapping of an eigenfunction can be understood as its exponential decay inside the branches. We describe a general variational formalism for detecting trapped modes in such resonators. For finite waveguides with general cylindrical branches, we obtain a sufficient condition which determines the minimal length of branches for getting a trapped eigenmode. Varying the branch lengths may switch certain eigenmodes from non-trapped to trapped or, equivalently, the waveguide state from conducting to insulating. These concepts are illustrated for several typical waveguides (L-shape, bent strip, crossing of two strips, etc.). It was also concluded that the well-established theory of trapping in infinite waveguides may be incomplete and require further development for applications to finite-size microscopic quantum devices.

1.2.1 Connected curved waveguides, mesoscopic systems

One could consider a pair of parallel straight quantum waveguides coupled laterally through a window of a width l in the common boundary. The authors of [21] showed that such a system has at least one bound state. We find the corresponding eigenvalues and eigenfunctions numerically using the modematching method, and discuss their behavior in several situations. They also discussed the scattering problem in this setup, in particular, the turbulent behavior of the probability flow associated with resonances. The level and phaseshift spacing statistics shows that in distinction to closed pseudointegrable billiards, the present system is essentially nonchaotic.

A strong motivation to study such bound states and related resonance effects comes from recent developments in semiconductor physics, because they can be used as models of electron motion in socalled quantum wires, i.e., tiny strips of a very pure semiconductor material, and similar structures. Let us briefly recall key features of such systems. Characteristic properties of the semiconductor microstructures under consideration are small size, typi-

cally from tens to hundreds of nm, high purity, which means that the electron mean free path can be a few μm or even larger, and crystallic structure. In addition, boundaries of the microstructures consist usually of an interface between two different semiconductor materials; the electron wavefuction are known to be suppressed there. Behavior of an electron in such a mesoscopic system structure is, of course, governed by the manybody Schródinger equation describing its interaction with the lattice atoms including the boundary, external fields, and possible impurities. The mentioned properties allow, however, to adopt several simplifying assumptions. As we have said the mean free path is typically two or three orders of magnitude greater than the size of the structure; hence the electron motion can be assumed in a reasonable approximation as ballistic, i.e., undisturbed by impurity scattering.

1.2.2 Bound states in twisting tubes

Here we should also add a paper by J. Goldstone and R. L. Jaffe [23]. It is easy to see that the uncertainty principle can pro- vide binding in quantum systems. Consider, for example, an infinite cylindrical tube with a bulge in the middle. A particle constrained to move in this tube can have lower transverse momentum and therefore lower transverse energy within the bulge, where it is less severely confined. A bound state results because the quantum particle would have to squeeze into the cylindrical section of the tube in order to propagate away to infinity. Such a system a straight tube with a slowly changing radius can be mapped into a one-dimensional problem in which the changing radius appears as a changing potential. A bulge corresponds to attraction, and in one dimension an attraction, no matter how weak, suffices to produce binding.

The object of this paper is to demonstrate that bends do as well as bulges. It has been proved that an infinite tube with a constant normal cross section always has a bound state if it bends. Apparently, a bend provides a region in which the quantum particle can relax, lowering its momentum in comparison with straight regions, though this is not as obvious as it is for bulges.

1.2.3 Kirchhoffs Rule for Quantum Wires

One particle quantum scattering theory on an arbitrary finite graph with n open ends and where we define the Hamiltonian to be (minus) the Laplace operator with general boundary conditions at the vertices. This results in a scattering theory with n channels has been observed in [24]. The corresponding on-shell S-matrix formed by the reflection and transmission amplitudes for incoming plane waves of a negative energy explicitly was given in terms of the boundary conditions and the lengths of the internal lines. It appears to be unitary, which may be viewed as the quantum version of Kirchhoffs law. The system exhibits covariance and symmetry properties. It is symmetric if the boundary conditions are real. Also there is a duality transformation on the set of boundary conditions and the lengths of the internal lines such that the low energy behavior of one theory gives the high energy behavior of the transformed theory. Finally we provide a composition rule by which the on-shell S-matrix of a graph is factorizable in terms of the S-matrices of its subgraphs. All proofs only use known facts from the theory of self-adjoint extensions, standard linear algebra, complex function theory and elementary arguments from the theory of Hermitian symplectic forms.

1.3 Novel numerical methods development

Recently this problem has given a boost to the development of a number of novel numerical methods [25], where the autohers surveyed various numerical methods for finding solutions of quantum confined states, especially considering states in two-dimensional (2D) tubes, or 2D surfaces that are confined in the transverse direction but are unconfined in the longitudinal direction. We first review existence proofs for bound states in long 2-D tubes. They also reviewed various methods for finding such states and we discuss the significance of these eigenstates.

When inventing problems for introductory courses in quantum mechanics, it is common for instructors to avoid the complications of space-dependent potentials by dealing with motion in a region with constant (i.e., zero) po-

tential, bounded by hard walls. By doing so, one can focus on the effects
of the boundary conditions on the solutions. Thus, the student typically
begins with a one-dimensional box, after which he/she can study a box in
two or three dimensions. As we will show in this article, solutions on two-
dimensional surfaces exhibit a number of interesting quantum properties,
symmetries, and degeneracies. In this paper, we consider a number of simple
two-dimensional (2D) hard-wall geometries, which can be straightforwardly
solved numerically by undergraduates, and we give examples of the types of
solutions that can be demonstrated for such systems. One example of a 2D
system that has been widely investigated is a 2D region where a particle is
confined to a cavity. Such systems have a direct analog with electromagnetic
waves in a 2D cavity. For electrons moving in a 2D cavity in a quantum
heterostructure, such a state is commonly referred to as a quantum dot.1 In
this paper, our emphasis will be on particles moving in long tubes or chan-
nels, where the particle is confined in the transverse direction but can move
freely in the longitudinal direction. Such states for electrons in quantum
heterostructures are referred to as quantum wires or electron waveguides".
It has been relatively recently understood that under a rather general set
of conditions, confined modes will exist in these 2D tubes, despite the fact
that confined modes would not exist for classical particles in such a system.2
As we will show, any localized bulge or bend in an otherwise straight chan-
nel or quantum wire will give rise to a stationary state which has a lower
energy than the threshold energy for free motion down the channel; the cor-
responding wave function is thus localized. Two popular textbooks have
posed problems dealing with these states, but the approaches used in these
problems involved variational methods or limiting cases, which are sufficient
to demonstrate the existence of a confined mode but which can give a rather
poor value for the energy. In this paper we discuss various numerical meth-
ods by which one can obtain accurate answers, and in certain cases extremely
precise values, for the eigenstates in simple geometries.

Chapter 2

Statement of the problem

2.1 S-type skew symmetric cross-wire system: motivation and reasoning

With the advance of fine-line lithography, devices can now be made which conduct along two-dimensional surfaces shaped into channels the width of which can be as narrow as $75\,nm$. Configured in four terminal junctions, such quantum wires are used to investigate quantum interference effects.

We introduce a skew-symmetric quantum wire intersection, as shown in Fig.[2.1], such that one of the two wires is straight, whereas the other one is curved. This system is more likely to posses a quantum bound state, compared to the other types of geometry.

Since for the configurations we consider there is no trapping classically, the presence of a localized quantum mechanical state is not an obvious phenomenon. It shows the quantum binding of a classically unbound system, and thus complements the phenomenon of the decay of a classically bound state by quantum tunneling. The problem is distinct from open geometries explored previously, such as that where the conducting region is contained by hyperbolas $x^2y^2 = \mathrm{const}$. Because of the "pinched-off" arms of that shape, there are an infinity of classical periodic orbits, so that the presence there of quantum bound states is not surprising. We return to this point later. We believe that the detailed shape of the potential which confines the electron
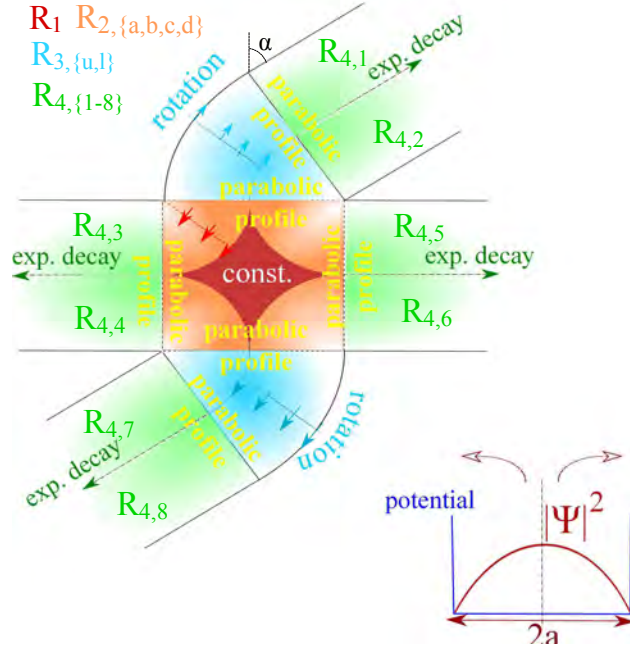
Figure 2.1: Schematic diagram of the potential formed by the crossed wires.

to the channel is not important in determining the qualitative fact of the presence of a bound state at the intersection. We take a potential which is zero inside the channels and infinite outside, so that the Hamiltonian is

$$\mathcal{H} = \frac{p^2}{2m^*} \tag{2.1}$$

inside the well, with the boundary condition that the electron's wave function goes to zero on the sides of the channel. We have used two methods to calculate the bound-state energy and wave function and describe them in the following paragraphs. One of these methods is also suitable for extension to the propagating case, and we show results from such calculations.

We also are looking for a different type of solution in the "arms" or "sleeves" away from the central square. Once the influence of the other arm is negligible, the problem becomes identical to one-dimensional infinite potential well with well known $\sin(\pi x/(2a))$. Thus we seek the solution with a parabolic profile which provides a better description of the realistic quantum state compared to the "'trianlge" shape.

There could be two basic methods to calculate *numerically* the bound-state energy and wave function and describe them in the following paragraphs. One of these methods is also suitable for extension to the propagating case, and we show results from such calculations. We conclude with some remarks on other configurations, and on the two-electron case. Schematic diagram of the potential formed by the crossed wires is the following: The hatched area, together with symmetry statements, is sufficient to display information about the bound-state wave functions and is the area shown in Fig. 2. The regions I through V are used in our function expansion method. The origin of the x and y axes is taken to be located at the lower left corner of region V. The system obviously possesses *four-fold rotational symmetry.*

The wave function goes to zero on the sides of the channel (see Fig. 2.1). Two methods are used to calculate the bound-state energy and wave function. The first model is a mesh point method in which the Authors replace the Schrödinger equation

$$H\psi = E\psi \tag{2.2}$$

by a difference equation for the wave function evaluated on a rectangular mesh of points in the plane of wires with discrete evolution in a "pseudotime" variable, t [39]. This equation is the discretized version of the differential equation

$$\delta\Psi/\delta t = \Delta\Psi, \tag{2.3}$$

where Δ is the Laplacian operator. Then the difference equation is given, which was iterated until Ψ becomes an eigenfunction of the discretized Δ operator. When the initial wave function is taken to be symmetric about the center lines in the x and y directions and about the diagonal line $x = y$, the eigenvalue found below the propagation threshold with the corresponding energy $E = 0.66E_t$, where $E_t = \hbar^2(\pi/w)^2/(2m^*)$ is the threshold energy, w is the width of the channel.

2.2 Variational principle and formalism

Variational principle, or Rayleigh-Ritz principle, is an approximation method of calculations of the one-particle eigenvalues (mostly, the *ground state*), different from the perturbation method [26].

Let $|\Psi_n\rangle$ be the eigenstate of $\mathcal{H}$. We introduce some normalized nearby state $|\Psi\rangle$

$$|\Psi\rangle = |\Psi_n\rangle + |\delta\Psi\rangle \tag{2.4}$$

so that $\langle\Psi|\Psi\rangle = 1$. This means that if $|\Psi_n\rangle$ is a complete orthonormal set of the eigenstates of $\mathcal{H}$, then

$$|\Psi\rangle = |\Psi_n\rangle + |\delta\Psi\rangle = N|\Psi\rangle + \sum_{n\neq m} \epsilon_m|\Psi_m\rangle \tag{2.5}$$

for some small numbers ϵ_m. Let $\mathcal{E}$ be the expectation value of $\mathcal{H}$ in $|\Psi\rangle$. The main idea of the variational method is that the change of $\mathcal{E}$ due to the ϵ_m vanishes in the first order:

$$\delta\mathcal{E} = \langle\Psi|\mathcal{H}|\Psi\rangle - \langle\Psi_n|\mathcal{H}|\Psi_n\rangle = \langle\Psi_n|\mathcal{H}|\delta\Psi\rangle + \langle\delta\Psi|\mathcal{H}|\Psi_n\rangle + \langle\delta\Psi|\mathcal{H}|\delta\Psi\rangle \tag{2.6}$$

The sate is normalized, $\langle\Psi|\Psi\rangle = 1$. Therefore,

$$\langle\delta\Psi|\Psi\rangle + \langle\Psi|\delta\Psi\rangle = \delta\langle\Psi|\Psi\rangle = 0. \tag{2.7}$$

Ground state is the most important case. Let $|\Psi_0\rangle$ - ground state and it is not degenerate. Then $\mathcal{H}|\Psi\rangle = E_1^0|\Psi_0\rangle$.

$$\langle\Psi|\mathcal{H}|\Psi\rangle = \sum_n E_n|\langle\Psi|\Psi_n\rangle|^2 \geq \sum_n E_1^0|\langle\Psi|\Psi_n\rangle|^2 = E_1^0\langle\Psi|\Psi\rangle = E_1^0 \tag{2.8}$$

The ground state is a **true minimum**. Our solution is based on this fact.

2.3 Existence of a quantum bound state in a rectangular crossed-wire system

Now we present a solution to a simpler considered problem, originally suggested by Krishna Rajagopal in 1974. The ground state energy is below the lowest possible propagating state energy, therefore the existence of a quantum bound state is confirmed. We demonstrate the existing solution of the cross-shaped infinite region based on [2].

2.3.1 Previously used trial function by K.Rajagopal

We start with Schród́inger equation for the considered geometry:

$$-\frac{\hbar^2}{2m}\left(\frac{\partial^2\Psi(x,y)}{\partial x^2} + \frac{\partial^2\Psi(x,y)}{\partial y^2}\right) = \mathbb{E}\Psi(x,y) \qquad (2.9)$$

Following the variable separation procedure, we look for the solution in the following form:

$$\Psi(x,y) = \mathbb{X}(x)\mathbb{Y}(y)\,. \qquad (2.10)$$

This results in the following expression:

$$\mathbb{Y}\frac{\partial^2\mathbb{X}}{\partial x^2} + \mathbb{X}\frac{\partial^2\mathbb{Y}}{\partial y^2} = -\frac{2m\mathbb{E}}{\hbar^2}\mathbb{X}\mathbb{Y}\,, \qquad (2.11)$$

being split into two separate equations:

$$\frac{d^2\mathbb{X}}{dx^2} = -k_x^2\mathbb{X} \qquad (2.12)$$

$$\frac{d^2\mathbb{Y}}{dy^2} = -k_y^2\mathbb{Y} \qquad (2.13)$$

with $k_x^2 + k_y^2 = \frac{2m\mathbb{E}}{\hbar^2}$. The general solution to Eq.2.13 is $\mathbb{Y}(y) = \mathcal{C}_1\cos k_y y + \mathcal{C}_2\sin k_y y$, and, in order to satisfy the boundary conditions $\mathcal{Y}(\pm a) = 0$, we need to assume $k_y = n\frac{\pi}{2a}$ with its minimal value $k_y = \frac{\pi}{2a}$. Therefore, the

propagating particle energy must satisfy

$$\mathcal{E} \geq \frac{\hbar^2}{2m} \left(k_x^2 + \frac{\pi^2}{4a^2} \right) \tag{2.14}$$

We conclude that every state with its energy eigenvalues being *less then the critical energy*:

$$\mathbb{E}_{cr} = \frac{\pi^2 \hbar^2}{8ma^2} \tag{2.15}$$

represent a **bound state**.

Here we address a trial function for our problem, first suggested by Krishna Rajagopal in 1974 [2]:

$$\begin{cases} \left(1 - \frac{xy}{a^2}\right) \mathsf{e}^{-\alpha} & |x| < a \,\&\&\, |y| < a \\ \left(1 - \frac{x}{a}\right) \mathsf{e}^{-\alpha|y|} & |x| < a \,\&\&\, |y| > a \\ \left(1 - \frac{y}{a}\right) \mathsf{e}^{-\alpha|x|} & |x| > a \,\&\&\, |y| < a \\ 0 & \text{otherwise} \end{cases} \tag{2.16}$$

Obviously, the function is continuous and drops to zero in the boundaries, and therefore satisfies all the requirements for a wave function. However, the first derivative of this trial function is broken along certain lines, referred to as **roof lines**.

2.3.2   Solution based on variational principle

Here we briefly review the solution for the ground state energy corresponding to the previously considered K.Rajagopal trial function.

We note that generally the solution consists of three parts - normalization of the wave function, bulk integration as well as the *roof lines* integration. While the first two steps are rather straightforward, the roof-line part requires special integration techniques, involving generalized function properties. We are going to develop general integration method, leading to the roof-line integrals for both Rajagopal and S-type trial functions. This method will be elaborated in details in Appendix A. As for now, we will just summarize the

results, as it was presented in [2].

First, we not that the whole interior of the cross-shaped region consists of 8 pairs of distinct regions, triangular 1/8 symmetric cut of the central square and a half of each sleeve (this parts will be referred to as "1" and "2"). The normalization condition could be now presented as:

$$8\left(\mathbb{I}_1 + \mathbb{I}_2\right) = 1 \tag{2.17}$$

with the probability density evaluated as follows:
Part "1":

$$\mathbb{I}_1 = \frac{1}{2}\mathcal{A}^2 \int\limits_{x=0}^{a}\int\limits_{y=0}^{a}\left(1 - \frac{x\,y}{a^2}\right)^2 \mathsf{e}^{-2\gamma}dxdy = \frac{11}{36}\mathcal{A}^2 a^2 \mathsf{e}^{2\gamma} \tag{2.18}$$

and *Part "2"*:

$$\mathbb{I}_2 = \mathcal{A}^2 \int\limits_{x=a}^{\infty}\int\limits_{y=0}^{a}\left(1 - \frac{x}{a}\right)^2 \mathsf{e}^{-2\gamma x/a}dxdy = \mathcal{A}^2 a^2 \frac{\mathsf{e}^{-2\gamma}}{6\gamma}\,. \tag{2.19}$$

These equations lead to the following normalization condition:

$$8\left(\frac{\mathcal{A}^2 a^2}{6\gamma}\mathsf{e}^{-2\gamma} + \frac{11}{36}\mathcal{A}^2 a^2 \mathsf{e}^{-2\gamma}\right) = 1 \tag{2.20}$$

and, finally,

$$\mathcal{A} = \sqrt{\frac{9\gamma}{2a^2}\frac{\mathsf{e}^{2\gamma}}{6 + 11\gamma}} \tag{2.21}$$

Now we calculate the ground state (average kinetic) energy:

$$\langle\mathcal{H}\rangle = -\frac{\hbar^2}{2m}\langle\Psi(x,y)|\frac{\partial^2}{\partial x^2} + \frac{\partial^2}{\partial y^2}|\Psi(x,y)\rangle = -8\frac{\hbar^2}{2m}\left(\mathcal{J}_1 + \mathcal{J}_2\right), \tag{2.22}$$

where $\mathcal{J}_1$ vanishes:

$$\mathcal{J}_1 = \frac{1}{2}\mathcal{A}^2 \int_0^a \left(1 - \frac{xy}{a^2}\right)\left(\frac{\partial^2}{\partial x^2} + \frac{\partial^2}{\partial y^2}\right)\left(1 - \frac{xy}{a^2}\right)\mathsf{e}^{-\gamma}dxdy = 0\,. \qquad (2.23)$$

In contrast, $\mathcal{J}_2$ term is as follows:

$$\mathcal{J}_2 = \mathcal{A}^2 \int_{x=a}^\infty \int_{y=0}^a \left(1 - \frac{y}{a}\mathsf{e}^{-\gamma x/a}\right)\left(\frac{\partial^2}{\partial x^2} + \frac{\partial^2}{\partial y^2}[= 0]\right) \qquad (2.24)$$

$$\left(1 - \frac{y}{a}\mathsf{e}^{-\gamma x/a}\right)dxdy = \frac{1}{6}\mathcal{A}^2\gamma\mathsf{e}^{2\gamma}$$

We add up all the results, and without the roof lines the ground state energy is:

$$\langle \mathcal{H}\rangle - -\frac{2}{3}\mathcal{A}^2\frac{\hbar^2\gamma}{m}\mathsf{e}^{-2\gamma} \qquad (2.25)$$

Now we summarize the results for the roof line integration.

The roof lines in this case are classified as follows:

- right arm central symmety line ($\times 8$) K_1 ;

- central square symmetry lines - $\mathcal{K}_2$;

- central square boundary lines - $\mathcal{K}_1$;

After the applying generalized funciton properties, the integration results are as follows:

$$\mathcal{K}_1 = \frac{2\hbar^2}{m\gamma}\mathsf{e}^{-2\gamma}\mathcal{A}^2 \qquad (2.26)$$

$$\mathcal{K}_2 = \frac{2\hbar^2}{m}\mathsf{e}^{-2\gamma}\mathcal{A}^2 \qquad (2.27)$$

$$\mathcal{K}_3 = \frac{2\hbar^2}{2m}\left(3\gamma - 1\right)\mathcal{A}^2 \qquad (2.28)$$

Finally, after taking into account all the required components and the

proper normalization, the

$$\langle \mathcal{H} \rangle = \frac{3\hbar^2}{ma^2} \frac{\gamma^2 + 2\gamma + 3}{6 + 11\gamma} \tag{2.29}$$

Consequently, we are looking to the variational parameter γ value, minimizing the ground state energy:

$$\frac{d\langle \mathcal{H} \rangle}{d\gamma} = 0 \,. \tag{2.30}$$

Here we are obviously looking for a minimum, the maximum does not exist. This minimum condition (Eq.2.30) results in

$$(6 + 11\gamma)(2\gamma + 2) = 11(\gamma^2 + \gamma + 3) \tag{2.31}$$

and

$$\gamma = \frac{-6 + \sqrt{36 + 21}}{11} \qquad \gamma = 0.940 \tag{2.32}$$

and the corresponding energy is

$$\mathbb{E}_0 = \langle \mathcal{H} \rangle = \frac{3\hbar^2}{ma^2} \frac{3(\gamma + 1)}{11} = \frac{6}{11} \frac{\hbar^2}{m\gamma^2} (\gamma + 1) = 1.058 \frac{\hbar^2}{ma^2} \tag{2.33}$$

This result is obviously an approximation. The true value of the ground state energy is **less** than $\mathbb{E}_0$. However, the obtained energy values is below the threshold energy obtained in the previous section:

$$\mathbb{E}_{cr} = \frac{\pi^2}{8} \frac{\hbar^2}{ma^2} = 1.2337 \frac{\hbar^2}{ma^2} \tag{2.34}$$

Consequently, the existence of a **quantum bound state is proved**. As the next step, we will present a novel trial wave function, leading to a lower ground state energy value.

Chapter 3

S-type skew symmetric crossed wires: ground state

In this Chapter, the calculations are discussed to determine whether quantum effects can cause the trapping of an electron at the intersection of S-type skew symmetric cross-wire system. The sketch of the system is shown in Fig.3.1. Such electron trapping could modify considerably the operation of devices made of these wires by changing their transport and optical properties, such as electron mobility and localization parameters, that are important for optical sensing in particular.

The principle problem here is to develop a new trial function that would lead to a lower value of the ground state energy, and then to calculate the corresponding bound state energy of the system. Obviously, the wave function must be smooth (the function itself and its first derivative must both be continuous), otherwise quantum current can not be defined correctly. The point is that one or a few spatial derivatives (the gradient components) of the wave function is an essential and necessary part of the current definition in Quantum Mechanics. Consequently, the current cannot be calculated if the wave function is not smooth due to the non-existence of the wave function first derivatives in some directions. However we consider a stationary states calculations with no current here and so in our trial wave function there could be lines of discontinuity of the first derivative. The latter will

be referred to as "roof lines" in what follows. Roof lines, or lines with the discontinuous spatial derivative of the wave function, are the central point here. The system behavior along these lines is clearly unphysical since the first derivative of the wave function does not exist. In principle this leads to singularities (non-standard behavior) of a quantum current, but this does not affect the bound state calculations with no current we are interested in. Also such regions (or lines) are normally associated with δ-function (infinite) type of potential, which has nothing to do with the potential profile of our problem on the wave function spatial domain.

We do try to minimize the number and the impact of the roof lines in our variational model. To this end, we are looking for a better type of solution in the arms (or sleeves) away from the central square (see Fig.3.1), where the influence of the other arm is negligible and so, the problem becomes identical to one-dimensional infinite potential well with the well-known ground state wave function solution of the form $\sqrt{1/a}\sin[x/(2a)]$ ($2a$ is the sleeve width). The simplest wave function profile to mimic this behavior is the parabolic profile which we chose over here to provide a better description to the realistic quantum state.

3.1 The trial wave function

First, we specify all regions, where the wave function is specified by a separate formula (see Fig.3.1):

R_1 **(central curved rhombus)**

The region of the highest probability density is as follows;

$$\begin{cases} (|x| - a)^2 + (|y| - a)^2 > a^2 \\ |x| < a \\ |y| < a \end{cases}$$

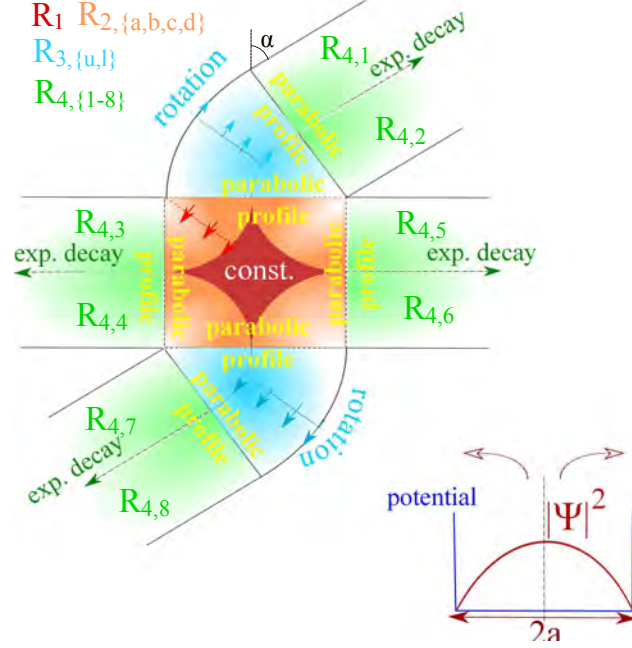with the constant wave function

Figure 3.1: General schematics and geometry of the problem with finite inclination angle α. The regions of the different wave function spatial dependence are specified by different colors.

$$\Psi_1(x, y) = \mathcal{N} \mathsf{e}^{-\gamma} = \text{const} , \tag{3.1}$$

Since the region is considerably larger compared to the case of Rajagopal wave function, our present normalization constant is expected to exceed the previously established normalization:

$$\mathcal{N}^{Rj} = \sqrt{\frac{9\gamma}{2a^2} \frac{\mathsf{e}^{2\gamma}}{11\gamma + 6}} \tag{3.2}$$

R_2 (four quarter-circles)

The remaining part of the central square could be specified as

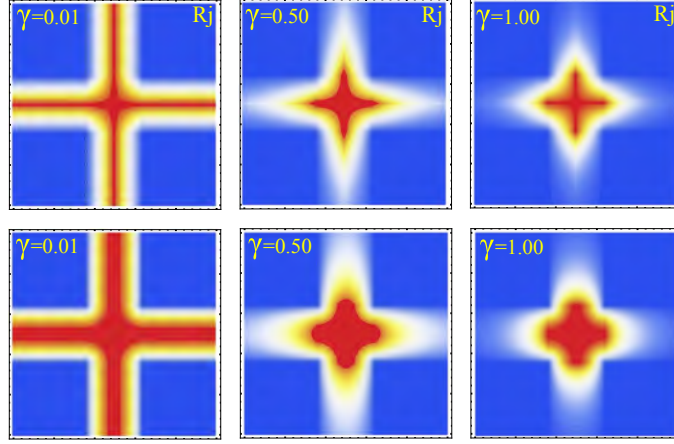$$\begin{cases} (|x| - a)^2 + (|y| - a)^2 < a^2 \\ |x| < a \\ |y| < a \end{cases} \tag{3.3}$$

Figure 3.2: Roof line, representing the beginning of the exponential decay. The wave function is demonstrated for x of the range from $-0.92\,a$ to $0.92\,a$, and y - from 0 to $2.24\,a$. The wave function is presented as a density plot using Temperature colormap, in which the red color corresponds to the highest probability density and the blue one - to the lowest. This convention is adopted for all the density plots in the present Thesis.

with another wave function

$$\Psi_2(x, y) = \mathcal{N}\left(1 - \left(1 - \frac{\Delta}{a}\right)^2\right)\mathsf{e}^{-\gamma} \tag{3.4}$$

$$\Delta = \sqrt{(a - |x|)^2 + (a - |y|)^2} \tag{3.5}$$

so the wave function depends only on the distance from the adjoining vertex of the central square. Obviously, the function is isotropic (no angular dependence) in the translated coordinates.

R_3 (two circular segments)

- The upper circular segment (C.S.) is located in the following region:

$$\begin{cases} y > a \\ y < -Tx + a(1 + T) \\ (x - a)^2 + (y - a)^2 < (2a)^2, \end{cases} \tag{3.6}$$

- the lower one:

$$\begin{cases} y < -a \\ y > -Tx - a(1+T) \\ (x+a)^2 + (y+a)^2 < (2a)^2 \end{cases} \tag{3.7}$$

where $T = \tan\alpha$ and $C = 1/T = \cot\alpha$. The corresponding wave function is given as:

$$\Psi_3(x,y) = \mathcal{N}\left(1 - \left(1 - \frac{\Delta'}{a}\right)^2\right) e^{-\gamma} \tag{3.8}$$

$$\Delta' = \sqrt{(a \mp x)^2 + (a \mp y)^2} \,, \tag{3.9}$$

where the $\mp$ sign correspond to the upper and lower regions respectively, so that the corresponding vertices of the central square are $\{a, a\}$ and $\{-a, -a\}$. The dependence is very similar to that of R_2 region, however the wave function is equal to zero for both $\Delta' = 0$ and $\Delta' = 2a$ to ensure zero probability density at all boundaries (on the both sides).

R_4 (**Eight semi-infinite rectangles - ”sleeves”**)

At this point we need to account for the difference between the horizontal ($R_{4,\{3,4,5,6\}}$) and inclined vertical ($R_{4,\{1,2,7,8\}}$) sleeves.

The region R_4 consists of the *lower inclined sleeve*:

$$\begin{cases} y < -Tx - a(1+T) \\ y < cx - a(1-c) \\ y > cx - a(1 - c + 2\sqrt{1+c^2}) \end{cases} \tag{3.10}$$

and the *upper* one:

$$\begin{cases} y > -Tx + a(1+T) \\ y > cx + a(1-c) \\ y < cx + a(1 - c + 2\sqrt{1+c^2}) \end{cases} \tag{3.11}$$

We write the wave function in such way that the equations would represent similar coordinate dependence in the slanted $\{\xi, \eta\}$ local coordinate
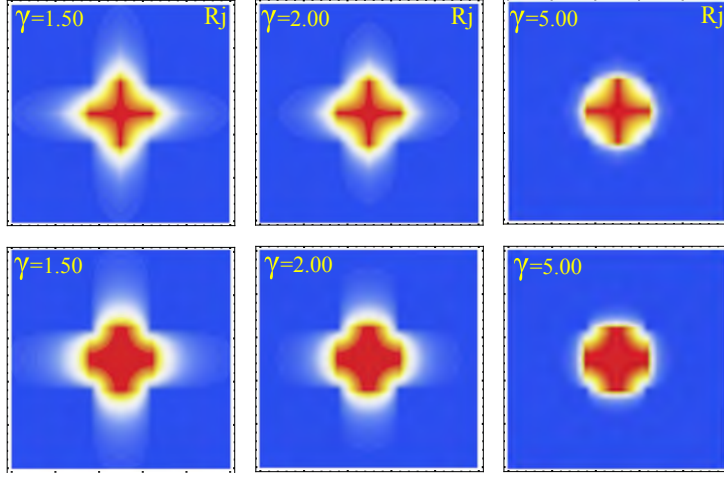
Figure 3.3: Spherical trial function with strong attenuation.

systems for each sleeve, presented at Fig.1:

$$R_{4,\{1,2\}} \Rightarrow \Psi_{4,\nearrow} = \mathcal{N} \left[1 - \left(\frac{\xi}{a} \right)^2 \right] e^{-\gamma(1+\eta/a)} \tag{3.12}$$

$$\xi = \frac{|-cx + y - a(1 - c + \sqrt{1 + c^2})|}{\sqrt{1 + c^2}} \tag{3.13}$$

$$\eta = \frac{|Tx + y - a(1 + T)|}{\sqrt{1 + T^2}} \tag{3.14}$$

and, in a similar manner:

$$R_{4,\{7,8\}} \Rightarrow \Psi_{4,\swarrow} = \mathcal{N} \left[1 - \left(\frac{\xi}{a} \right)^2 \right] e^{-\gamma(1+\eta/a)} \tag{3.15}$$

$$\xi = \frac{|-cx + y + a(1 - c + \sqrt{1 + c^2})|}{\sqrt{1 + c^2}} \tag{3.16}$$

$$\eta = \frac{|Tx + y + a(1 + T)|}{\sqrt{1 + T^2}} \tag{3.17}$$

In the case of a symmetric quantum dot ($\alpha = 0$):

$$R_{4,v} \Rightarrow \Psi_{4,v} = \mathcal{N} \left(1 - \left(\frac{x}{a} \right)^2 \right) e^{-\gamma|y|/a} \tag{3.18}$$

According to our model, only inclined vertical sleeves $R_{4,\{1,2,7,8\}}$ alter with angle α, whereas the horizontal sleeves $R_{4,\{3,4,5,6\}}$ are not modified (as well as the central square):

$$R_{4,h} \Rightarrow \Psi_{4,h} = \mathcal{N} \left(1 - \left(\frac{y}{a}\right)^2 \right) e^{-\gamma|x|/a} \qquad (3.19)$$

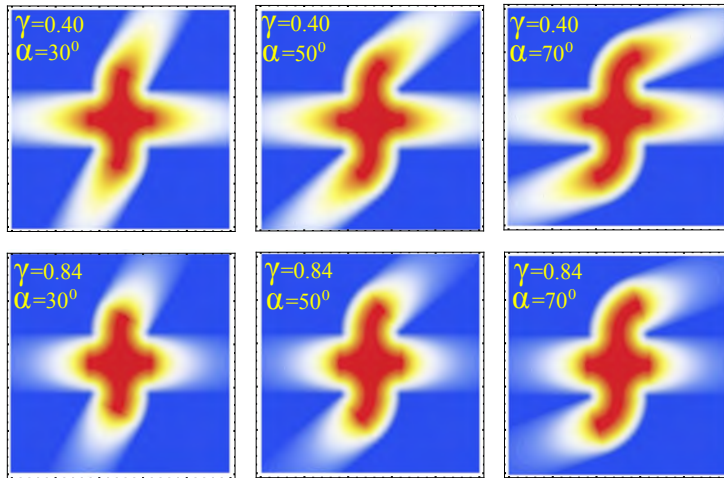One can easily verify that for $\alpha = 0$ the circular segments R_3 disappear

Figure 3.4: Density plot of the trial function for finite values of the inclination angle α. The plots are presented for three different angles $\alpha = 30^0$, 50^0 and 70^0 and for two values of the decay constant - $\gamma = 0.4$ and $\gamma = 0.7$, corresponding to the variational minimum of the Hamiltonian expectation value.

and the inclined vertical sleeves wave functions (3.12),(3.15) tend to the expression of the wave function in the vertical sleeve (3.18). These wave functions are different from the one obtained by Ragajopal as predicted.
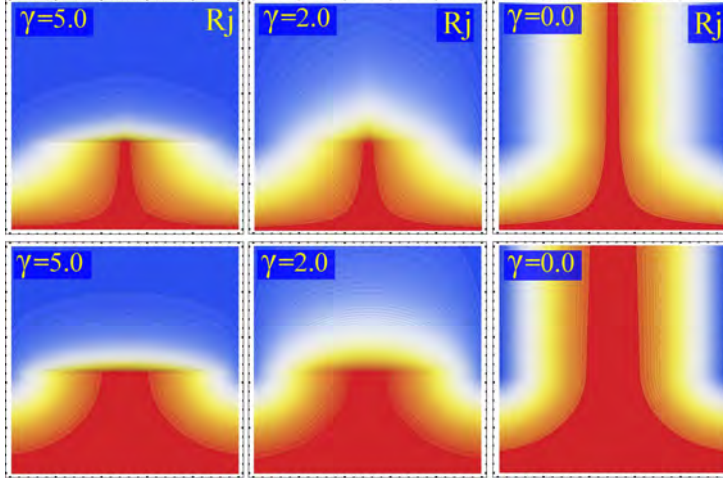
Figure 3.5: Roof line, representing the beginning of the exponential decay. The wave function is demonstrated for x of the range from $-0.92\,a$ to $0.92\,a$, and y - from 0 to $2.24\,a$.

3.2 Variational approach to the expectation values

In order to obtain the new normalization coefficient, we perform the integration of the probability density $|\Psi_i(x,y)|^2$.

R_1. The wave function $\Psi_1(x,y)$ is constant in the central curved rhombus. First, we need to obtain the area of R_1

$$A_1 = (2a)^2 - 4\left(\frac{1}{4}\pi a^2\right) = (4-\pi)a^2 \simeq 0.858a^2 \qquad (3.20)$$

and the corresponding probability density:

$$\Psi_1(x,y) = \mathcal{N}e^{-\gamma} \Rightarrow |\Psi_1(x,y)|^2 = \mathcal{N}^2 e^{-2\gamma} \qquad (3.21)$$

$$\mathcal{I}_1 = \int dx \int_{R_1} dy\, |\Psi_1(x,y)|^2 = \mathcal{N}^2 A_1 e^{-2\gamma} = (4-\pi)\mathcal{N}^2 a^2 e^{-2\gamma} \ .$$

R_2. Region R_2 consists of *four* equivalent quarter-circles. We demonstrate the result for the quarter-circle with the center at $\{a,a\}$, so that the contribution from R_2 region is expected to be $4\mathcal{I}_2$. Correspondingly, we find
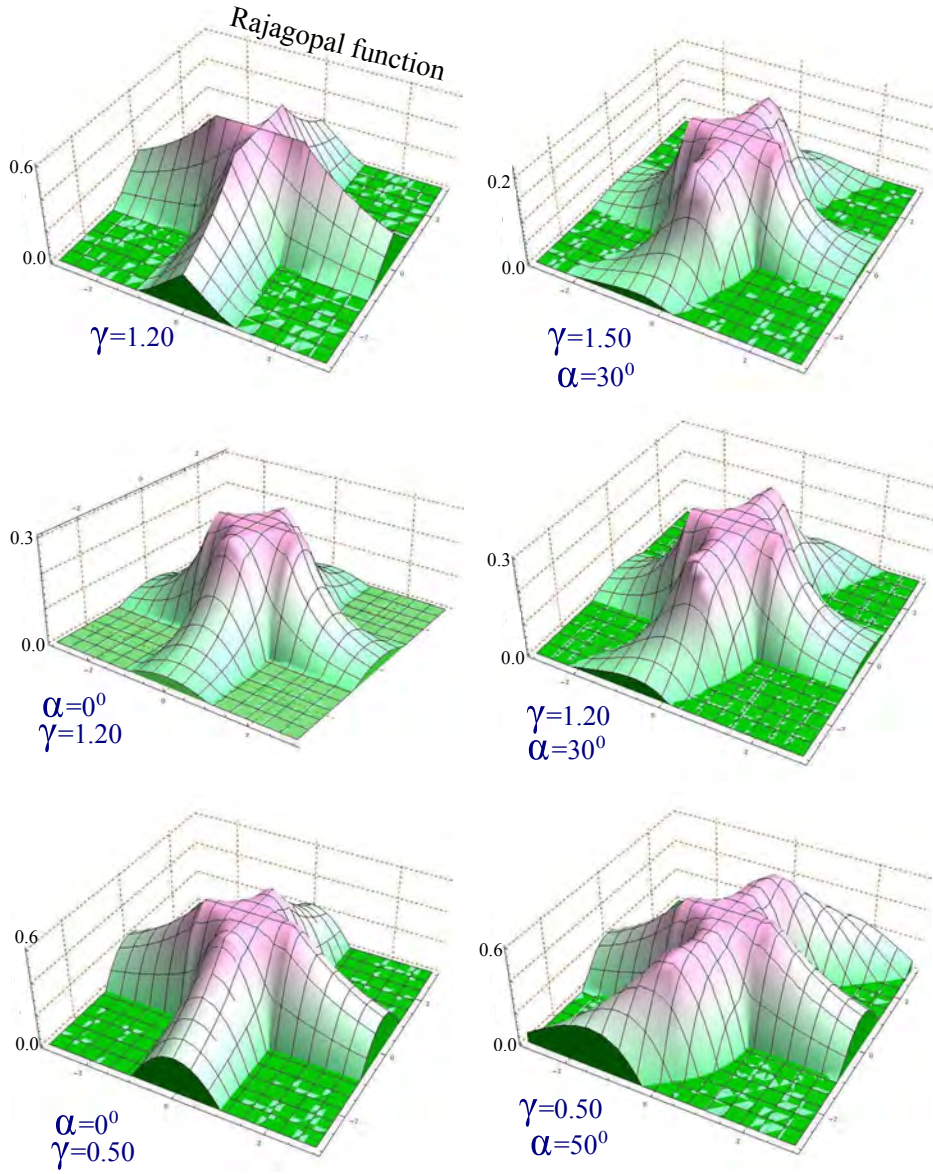
Figure 3.6: 3D plots of the new trial wave function.

the wave function integral:

$$\Psi_2(x,y) = \mathcal{N}\left(1 - \left(1 - \frac{r}{a}\right)^2\right)e^{-\gamma} \tag{3.22}$$

$$\mathcal{I}_2 = \mathcal{N}^2 \int\limits_0^a rdr \int\limits_0^{\pi/2} d\phi \left(1 - \left(1 - \frac{r}{a}\right)^2\right)^2 e^{-2\gamma} = \mathcal{N}^2 \frac{11}{60}\pi a^2 e^{-2\gamma},$$

where r is the distance from $\{a, a\}$-vertex of the central square to the point of observation for our choice of the sample region.

Region R_3 vanishes for $\alpha = 0$.

R_4. We consider a sample horizontal sleeve and keep in mind that the actual contribution of this region comes as $4\mathcal{I}_4$

$$\Psi_4(x, y) = \mathcal{N}\left(1 - \frac{y}{a}\right)\left(1 + \frac{y}{a}\right)e^{-\gamma|x|/a} \tag{3.23}$$

$$\mathcal{I}_4 = \int_{-a}^{a} dy \int_{a}^{\infty} dx \, |\Psi_4(x, y)|^2 = \mathcal{N}^2 \int_{-a}^{a} dy \int_{a}^{\infty} dx \left(1 - \left(\frac{y}{a}\right)^2\right)^2 e^{-2\gamma x/a} =$$

$$= \mathcal{N}^2 \frac{8a^2 e^{-2\gamma}}{15\gamma} \ .$$

The total integral now could be written as:

$$\mathcal{I} = \mathcal{I}_1 + 4\mathcal{I}_2 + 4\mathcal{I}_4 = \mathcal{N}^2\left[(4-\pi)a^2 e^{-2\gamma} + \frac{11}{15}\pi a^2 e^{-2\gamma} + \frac{32a^2 e^{-2\gamma}}{15\gamma}\right] = 1$$

$$\mathcal{N}^2 = \frac{15\gamma}{4a^2}\frac{e^{2\gamma}}{8 + (15 - \pi)\gamma} = \frac{3.75}{8 + 11.86\gamma}\frac{\gamma \, e^{2\gamma}}{a^2} \ .$$

Obviously, our normalization coefficient is expected to be considerably smaller than N^{Rj}. For $\gamma = 0.94$, leading to the variational minimum of the Hamiltonian expectation value for $\Psi^{Rj}(x, y)$, the normalization coefficient would be $\mathcal{N}^2 = 1.207/a^2$ in comparison to $(\mathcal{N}^{Rj})^2 = 1.697/a^2$.

3.2.1 Bulk Integration

Now we are at position to evaluate the expectation value of the Hamiltonian everywhere inside the cross. As a matter of fact, we need to account only for *two different* integrals $\mathcal{B}_2$ and $\mathcal{B}_4$, corresponding to R_2 and R_4 regions. The actual expression is as follows:

$$\langle \mathcal{H} \rangle_b = -\frac{\hbar^2}{2m}\left\langle \Psi_{(x,y)} | \frac{\partial^2}{\partial x^2} + \frac{\partial^2}{\partial y^2} | \Psi_{(x,y)} \right\rangle = -4\frac{\hbar^2}{2m}(\mathcal{B}_2 + \mathcal{B}_4) \tag{3.24}$$

Important. First, we note that the bulk integral $\mathcal{B}_1 = 0$, since the wave

function is constant in region R_1 (central rhombus). In spite of the fact that the components of the gradient (spatial derivatives) are not equivalent, the general *convex-concave symmetry* is not broken. In the case of Rajagopal trial function the situation is similar.

In each case we need to evaluate the following quantity:

$$\mathcal{B}_i = \int\limits_{R_i} dx\, dy\, \Psi_i(x, y) \left(\frac{\partial^2 \Psi_i(x, y)}{\partial x^2} + \frac{\partial^2 \Psi_i(x, y)}{\partial y^2} \right) \qquad (3.25)$$

since the wave function is always real. The latter statement also leads to the fact that any quantum-mechanical current for the suggested trial function is equal to zero everywhere in the system.

$\mathcal{B}_2$ - quarter-circles

Since the wave function $\Psi_2(\mathbf{r})$ has only radial dependence, it is advisable to take its Laplacian as well as the spatial integral in polar coordinates:

$$\Psi_2(\mathbf{r}) = \mathcal{N} \left(1 - \left(1 - \frac{r}{a} \right)^2 \right) e^{-\gamma} \qquad (3.26)$$

$$\nabla^2 \Psi_2(\mathbf{r}) = \frac{\partial^2 \Psi(r)}{\partial r^2} + \frac{1}{r} \frac{\partial \Psi(r)}{\partial r} = \mathcal{N} \frac{2}{a^2} \left(\frac{a}{r} - 2 \right) e^{-\gamma}$$

$$\mathcal{B}_2 = \int\limits_0^a r dr \int\limits_0^{\pi/2} d\phi \, \nabla^2 \Psi_2(\mathbf{r})\, \Psi_2(\mathbf{r}) = -\frac{1}{6} \mathcal{N}^2 \pi e^{-2\gamma}$$

$\mathcal{B}_4$ - semi-infinite rectangles (sleeves)

First, we evaluate the Laplacian of the trial function, considering one model upper vertical sleeve with $y > a$

$$\nabla^2 \Psi_4(x, y) = \mathcal{N} \nabla^2 \left[\left(1 - \frac{x^2}{a^2} \right) e^{-\gamma y/a} \right] = \mathcal{N} \frac{(\gamma^2 - 2)a^2 - x^2 \gamma^2}{a^4} e^{-\gamma y/a} \, . \qquad (3.27)$$

Here we first encounter the situation, where *both* $x-$ and $y-$ second derivatives are non-zero, namely, while the $\partial^2/\partial y^2$ is the result of the exponential decay (derivatives of all orders are non-zero); $\partial^2/\partial x^2$ reflects the *parabolic*

transversal profile of the wave function. The situation was not encountered with the Rajagopal trial function.

Consequently, the integral is in the form of

$$\mathcal{B}_4 = \int\limits_{-a}^{a} dx \int\limits_{a}^{\infty} dy \, \Psi_4(x,y) \nabla^2 \Psi_4(x,y) = 4\mathcal{N}^2 \left(\frac{2\gamma}{15} - \frac{1}{3\gamma} \right) \mathrm{e}^{-2\gamma} \qquad (3.28)$$

Also it is interesting to mention that here in contrast to $\Psi^{Rj}(x,y)$, the pure term (without normalization) $B_4/\mathcal{N}^2 \to \infty$ for $\gamma \to 0$, which corresponds to the infinite region of finite concavity of the sleeves. The singularity is compensated by the similar behavior of the wave function normalization.

Now we can summarize the results of the bulk integration:

$$\langle \mathcal{H} \rangle = -\frac{\hbar^2}{2m} \left\langle \Psi_{(x,y)} | \frac{\partial^2}{\partial x^2} + \frac{\partial^2}{\partial y^2} | \Psi_{(x,y)} \right\rangle = -4 \frac{\hbar^2}{2m} \left(\mathcal{B}_2 + \mathcal{B}_4 \right) = (3.29)$$
$$= -\mathcal{N}^2 \frac{\hbar^2}{15\gamma m} \left(16\gamma^2 - 5\pi\gamma - 40 \right) \mathrm{e}^{-2\gamma}$$

So far we just note that for $\gamma^{Rj} = 0.94$ we would obtain $\langle \mathcal{H} \rangle = +0.440 \, \mathcal{N} \, \hbar^2/m$, whereas for $\Psi^{Rj}(x,y)$ this term is purely negative for any value of γ.

3.2.2 Roof Line Integration

One of the most important features of the new trial wave function is minimal number and complexity of the roof lines. In fact, there is only one type of such line $\mathcal{L}_1$, associated with the beginning of the exponential decay in the sleeves.

We recall the analytic expressions of the function $\Psi_2(x,y)$ in the close vicinity of $\mathcal{L}_1$

$$\Psi_2(x,y) = \mathcal{N} \left(1 - (1 - \Delta/a)^2 \right) \mathrm{e}^{-\gamma}$$
$$\Delta = \sqrt{(a - |x|)^2 + (a - |y|)^2} \, , \qquad (3.30)$$

so we can expand it in terms of the small $x-$displacement from $\mathcal{L}_1$, namely $\delta_x = (a - x)/a$

$$\Psi_{x<a}(x, y) = \mathcal{N}\left[\left(1 - \left(\frac{y}{a}\right)^2\right) + \frac{y}{a - y}\delta_x^2\right]\mathsf{e}^{-\gamma}, \qquad (3.31)$$

Obviously the expansion is not valid at $y = \pm a$. The physical reason to that is that both components of the wave function gradient (spatial derivative) are not continuous However, the vertices of the central square do not give any contribution to any of the integrals since the wave function $\Psi_i(\pm a, \pm a) = 0$. Now the *generic wave function* next to $\mathcal{L}_1$ is presented as:

$$F_0(x, y) = \mathcal{N}\left\{\left(1 - \left(\frac{y}{a}\right)^2\right)\theta_{x>a} + \left[\left(1 - \left(\frac{y}{a}\right)^2\right) + \frac{y}{a - y}\delta^2\right]\theta_{x<a}\right\}$$

$$\times \exp\left[-\gamma\left(\theta_{x<a} + \frac{x}{a}\theta_{x>a}\right)\right].$$

Anzats. Since the only source of non-smooth C^0-type behavior is the beginning of the exponential decay, and we are collecting only δ-function terms, the sought second derivative could be written:

$$\mathcal{N}\left\{\left(1 - \left(\frac{y}{a}\right)^2\right)\theta_{x>a} + \left[\left(1 - \left(\frac{y}{a}\right)^2\right) + \frac{y}{a - y}\delta_x^2\right]\theta_{x<a}\right\}\times$$

$$\exp\left[-\gamma\left(\theta_{x>a} + \frac{x}{a}\theta_{x<a}\right)\right] \times \frac{\partial^2}{\partial x^2}\left[-\gamma\left(\theta_{x>a} + \frac{x}{a}\theta_{x<a}\right)\right]$$

$$F_0(x, y) = \mathcal{N}\left\{\left(1 - \left(\frac{y}{a}\right)^2\right)\theta_{x>a} + \left[\left(1 - \left(\frac{y}{a}\right)^2\right) + \frac{y}{a - y}\delta_x^2\right]\theta_{x<a}\right\}\times$$

$$\times \exp\left[-\gamma\left(\theta_{x<a} + \frac{x}{a}\theta_{x>a}\right)\right]$$

$$F_0(x \to a, y) = \mathcal{N}\left(1 - \left(\frac{y}{a}\right)^2\right)\mathsf{e}^{-\gamma}$$

The function is smooth (no roof lines) for $\gamma \to 0$, so we can write

$$\frac{\partial^2\Psi}{\partial x^2} = -\mathcal{N}\left(1 - \left(\frac{y}{a}\right)^2\right)\frac{\gamma\mathsf{e}^{-\gamma}}{a}\delta(x - a) \qquad (3.32)$$

$$\int\limits_{-a}^{a} dy \left(1 - \left(\frac{y}{a} \right)^2 \right)^2 = \frac{16a}{15} \tag{3.33}$$

The roof line integral could be expressed in the final form:

$$\mathcal{L} = 4 \cdot \left(-\frac{\hbar^2}{2m} \right) \mathcal{N}^2 \int\limits_{-a}^{a} dy \int\limits_{a-\epsilon}^{a+\epsilon} dx\, \Psi(x \to a, y) \frac{\partial^2 \Psi(x \to a, y)}{\partial x^2} \tag{3.34}$$

$$\mathcal{L} = \frac{2\hbar^2}{m} \mathcal{N}^2 \int\limits_{-a}^{a} dy \left(1 - \left(\frac{y}{a} \right)^2 \right)^2 \frac{\gamma e^{-2\gamma}}{a} = \frac{32}{15} \frac{\hbar^2}{m} \mathcal{N}^2 \gamma e^{-2\gamma} \tag{3.35}$$

3.3 Hamiltonian Expectation Values

3.3.1 Zero inclination angle

Now we find the Hamiltonian average as the sum of the *bulk* and the *roof* integrals:

$$\mathcal{B} = \left(-\frac{\hbar^2}{2m} \right) 4 \left(\mathcal{B}_2 + \mathcal{B}_2 \right) = -\frac{\hbar^2}{15\gamma m} \mathcal{N}^2 \left(16\gamma^2 - 5\pi\gamma - 40 \right) e^{-2\gamma} \tag{3.36}$$

and

$$\mathcal{L} = \frac{32\hbar^2}{15m} \mathcal{N}^2 \gamma e^{-2\gamma} \tag{3.37}$$

so that the expectation value:

$$\langle \mathcal{H} \rangle = \mathcal{B} + \mathcal{L} = \frac{\hbar^2}{m} \mathcal{N}^2 \frac{e^{-2\gamma}}{15\gamma} \left(16\gamma^2 + 5\pi\gamma + 40 \right). \tag{3.38}$$

Taking into account the normalization constant

$$\mathcal{N}^2 = \frac{15\gamma}{4a^2} \frac{e^{2\gamma}}{8 + (15 - \pi)\gamma} = \frac{3.75}{8 + 11.86\gamma} \frac{\gamma\, e^{2\gamma}}{a^2}, \tag{3.39}$$

we finally obtain

$$\langle \mathcal{H} \rangle = \frac{\hbar^2}{ma^2} \frac{16\gamma^2 + 5\pi\gamma + 40}{60\gamma - 4\pi\gamma + 32} \tag{3.40}$$

Applying the variational principle, we find the values of the exponential decay constant "gamma", corresponding to the minimum of the ground state energy. This results in $\gamma = 0.840$ and $\mathcal{E} = 0.898\hbar^2/(ma^2)$.
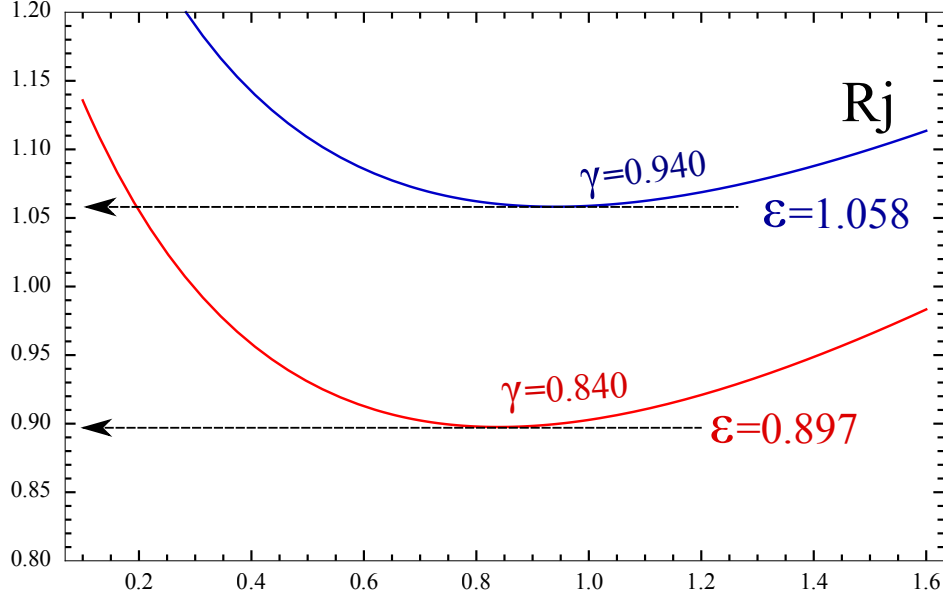

Figure 3.7: Energy expectation value as a function of the exponential decay γ, which is chosen as the variational parameter.

3.3.2 Finite non-zero inclination angle.

As we already mentioned, the number and the type of the roof lines are not altered in the case of y-asymmetric quantum dot. Correspondingly, we need to supplement the normalization with term $2 \times \mathcal{I}_3$, and bulk integrals - with $\mathcal{B}_3$ from region R_3:

$$\Psi_3(x,y) = \mathcal{N}\left(1 - \left(1 - \frac{\Delta'}{a}\right)^2\right)\mathsf{e}^{-\gamma}, \tag{3.41}$$

$$\Delta' = \sqrt{(a \mp x)^2 + (a \mp y)^2}, \tag{3.42}$$

so that the integrals

$$\mathcal{I}_3 = \mathcal{N}^2 \int\limits_0^\alpha d\phi \int\limits_0^{2a} r\,dr\, |\Psi_3(r)|^2 = \alpha e^{-2\gamma} \int\limits_0^{2a} \left(1 - \left(1 - \frac{r}{a}\right)^2\right)^2 r\,dr \quad (3.43)$$

$$\mathcal{I}_3 = \mathcal{N}^2 \frac{16}{15}\alpha a^2 e^{-2\gamma}$$

and

$$\nabla^2 \Psi_3(\mathbf{r}) = \frac{\partial^2 \Psi_3(r)}{\partial r^2} + \frac{1}{r}\frac{\partial \Psi_3(r)}{\partial r} = \mathcal{N}\frac{2}{a^2}\left(\frac{a}{r} - 2\right)e^{-\gamma} \qquad (3.44)$$

$$\int\limits_a^{2a} r\,dr \left[1 - \left(1 - \frac{r}{a}\right)^2\right]\frac{2}{a^2}\left(\frac{a}{r} - 2\right) = -\frac{8}{3} \qquad (3.45)$$

$$\mathcal{B}_3 = \int\limits_0^a r\,dr \int\limits_0^\alpha d\phi\, \Psi_2(\mathbf{r})\,\nabla^2 \Psi_2(\mathbf{r}) = -\mathcal{N}^2\frac{8}{3}\alpha e^{-2\gamma} \qquad (3.46)$$

and, finally,

$$-\frac{\hbar^2}{2m}\mathcal{B}_3 = +\frac{4}{3}\frac{\hbar^2}{m}\mathcal{N}^2\alpha\,e^{-2\gamma} \qquad (3.47)$$

Now we summarize all the terms,

$$\mathcal{I}_1 = \mathcal{N}^2(4 - \pi)a^2 e^{-2\gamma} \qquad (3.48)$$

$$\mathcal{I}_2 = \mathcal{N}^2\frac{11}{60}\pi a^2 e^{-2\gamma} \qquad (3.49)$$

$$\mathcal{I}_3 = \mathcal{N}^2\frac{16}{15}\alpha a^2 e^{-2\gamma} \qquad (3.50)$$

$$\mathcal{I}_4 = \mathcal{N}^2\frac{8}{15\gamma}a^2 e^{-2\gamma} \qquad (3.51)$$

so that

$$\mathcal{I} = \sum_\lambda \mathcal{I}_\lambda = 1 \qquad (3.52)$$

$$\frac{1}{\mathcal{N}^2} = \mathcal{I}_1 + \mathcal{I}_2 + \mathcal{I}_3 + \mathcal{I}_4 = \frac{4a^2}{15\gamma}\left(8 + \gamma(15 - \pi + 8\alpha)\right)e^{-2\gamma} \quad (3.53)$$

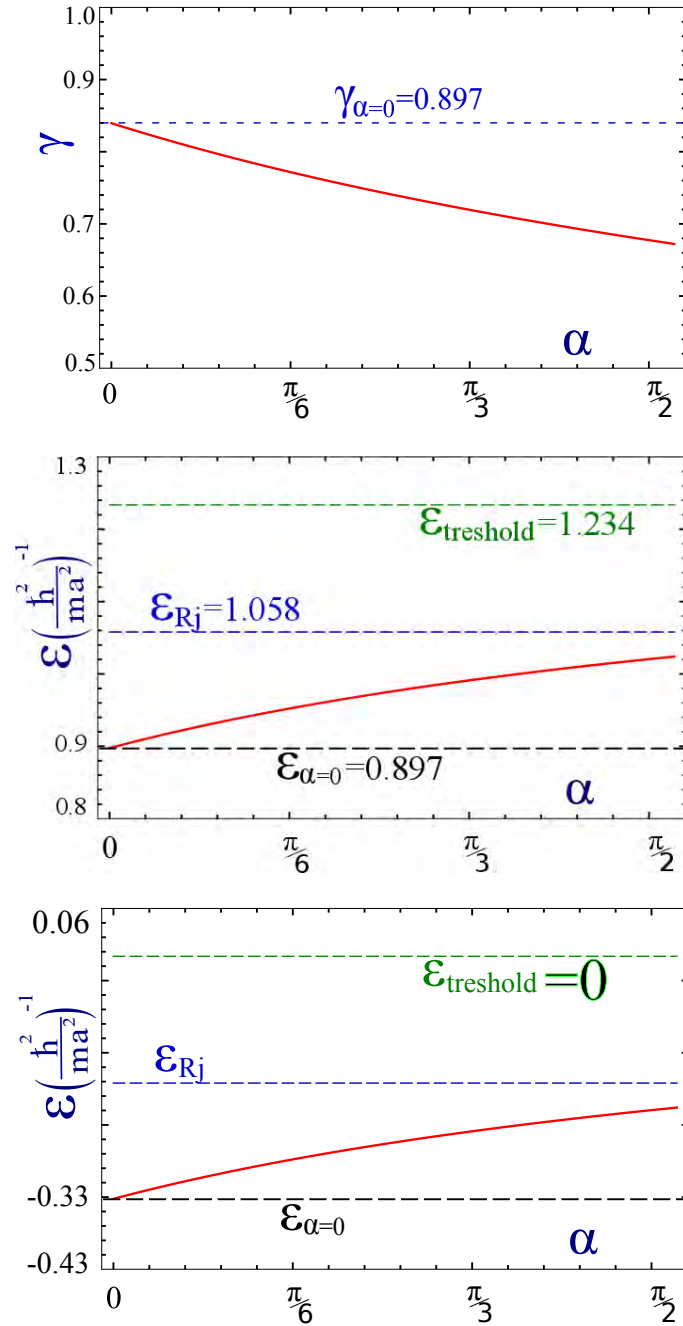The normalization constant $\mathcal{N}$ is, therefore, equal to:

Figure 3.8: Ground state energy for the skew symmetric cross-wired system. The upper panel shows how the variational minimum for the decay coefficient γ depends on the inclination angle α and the lower two plots represent the angular dependence of the ground state energy and the bound state energy respectively.

$$\mathcal{N} = \frac{\sqrt{15\gamma}}{2a} \mathrm{e}^{\gamma} \left(8 + \gamma(15 - \pi + 8\alpha)\right)^{-1/2} \tag{3.54}$$

The bulk and roof line integrals, therefore, give:

$$\langle \mathcal{H} \rangle = -\frac{\hbar^2}{2m} \mathcal{N}^2 \frac{1}{15} \left(5\pi + 8\left(5\alpha + \frac{5}{\gamma} + 2\gamma\right)\right) \mathrm{e}^{-2\gamma} \tag{3.55}$$

which result in the following final equation to determine the *ground state energy*:

$$\langle \mathcal{H} \rangle = \frac{\hbar^2}{4ma^2} \frac{5\pi\gamma + 8(5 + 5\alpha\gamma + 2\gamma^2)}{8 + \gamma(15 - \pi + 8\alpha)} \tag{3.56}$$

Now we are looking for the angular dependence of the variational minimum of the ground state energy. Since we chose the exponential decay coefficient γ to be that variational parameter, its angular dependence is now obtained by simple differentiation:

$$\frac{d\langle H(\alpha)\rangle}{d\gamma} = 0 \tag{3.57}$$

This results in the following angular dependence of γ:

$$\gamma = \frac{-32 - \sqrt{1024 - 4(10\pi - 75)(30 - 2\pi + 16\alpha)}}{2(30 - 2\pi + 6\alpha)} \tag{3.58}$$

Equation (3.58) provides the result for the exponential decay coefficient γ for an arbitrary value of the inclination angle α. These values of γ correspond to the variational minimum of the energy as a function of α. The obtained dependence, being one of our main results, is presented in Fig.3.8.

Having obtained all the relevant numerical results, we are at position to discuss its physical properties.

First, we can conclude that a finite inclination angle α leads to an increase of both **inverse** normalization constant $\mathcal{N}$ due to an extra finite region of non-zero wave function (see Fig.3.1) and the bulk integral term since another piece of a finite curvature is added. These regions were previously denoted as R_3 (upper and lower). Apart from that, here we are dealing with a new situation, where the variational minimum of the exponential decay coefficient γ varies with changing α. Correspondingly, in order to apply the variational

procedure, we re-derive the value of γ for each individual value of angle angle α.

The variational results for bound state energy are shown in Fig 3.8 at the two lower panels. We define the corresponding bound state energy as the difference between the obtained ground state energy and the minimal energy of a propagating state. According to our previous discussions, this critical energy is equal to $\epsilon_{treshold} = 1.234\hbar^2/(ma^2)$ (see Eq.(2.15)). We see that the ground state energy **increases** with the inclination α. This increase is finite, limited and does not reveal any singularities. Analyzing our results, we conclude that the binding energy decreases to approximately 2/3 of it initial value. It does not completely disappear, making the bound state possible for all values of the inclination angle. The obtained property makes the S-type skew symmetric system distinguished from the standard X-type.

3.4   Concluding remarks

Finalizing this thesis, I would like to emphasize the uniqueness and importance of the studied system. Indeed, there are very few structures, demonstrating quantum bound states in classically unbound systems. In this respect the problem definitely presents substantial interest from the theoretical point of view. Apart from that, simple two-channel geometry enables relatively accessible fabrication of tunable sensors based on the electronic, transport and optical properties of the S-type skew symmetric cross-wired system.

In this thesis, we have analyzed the angular dependence of the lowest energy bound state for an electron trapped at the intersection of two identical narrow channels (quantum wires) crossed at an arbitrary angle in such a way that the channel intersection area forms the square. When the channels are perpendicular, this is an unbound system, classically, that is known to possess a purely quantum single electron bound state [1]. Our task was to investigate the bound state energy as a function of the wire intersection angle, in order to find out whether the electron trapped state is still there for a non-zero inclination angle, and then to calculate the functional behavior of the bound

state energy as the channel intersection angle varies.

The very first main step we have done was to find a right trial function that solves the problem by means of the variational approach. Specifically, an analytical expression for the trial function was found and tested. The function is supposed to be smooth in the bulk, and it must drop down to zero at the boundaries. In addition, the so-called roof lines, the lines of discontinuous derivatives, have been found and characterized, and their contributions have been calculated using a special set of recipes.

Using the variational principle and the trial function established, the ground state energy of the problem has been calculated. This includes:

- finding the proper normalization constant of the accepted trial wave function,

- calculating the contributions to what of the bulk integrals and those of the roof lines. We used the exponential attenuation coefficient γ as the variational parameter, resulting in the lowest value of the ground state energy for any inclination angle α.

The bound state is present for any inclination angle α. The binding energy decreases with the increasing inclination angle α. However, the bound state persists for all accessible values of α, which is known not to be the case for other types of the wire intersection geometry. This is the central result of our work.

Our results have been compared with those obtained by using other (simpler) trial functions available in quantum mechanics texts. A qualitative agreement is demonstrated. The results of this thesis were presented with success at the annual American Physical Society meeting in Denver, CO, in March 2014 [49].

3.5 Research outlook

This is mostly a theoretical work, although it maintains certain approaches and patterns of numerical experiment, including visualizations and simulations using the Mathematica package.

The trial function found was then tested by using it in numerical simulations. It was demonstrated to result in the lowest possible ground state energy expectation value.

I would like to summarize briefly and to discuss the importance of the present thesis work, and also to point out its applications and possible future research directions. They are:

- This thesis work describes an important example of a quantum system, which is unbound in a classical sense, but yet it does possess a purely quantum bound state. The results are unique in that they give the angular dependence of the binding energy of the electron trapped at the skew-symmetric quantum channel intersection. This is something that was not reported before in the literature.

- The data and simulations, presented in this work, will be useful for the correct interpretation of electron transport peculiarities in realistic quantum systems such as semiconductor nanowire films and carbon nanotube bundles.

- The results obtained provide new useful information of relevance to the properties of semiconductor quantum dot-like systems and other devices of confined geometries. Understanding the properties of quantum confined systems is important for the development of a variety of applications in modern nanotechnology. For example, a bound quantum state in an S-type skew symmetric cross-wire system could potentially be used to control electron transport on the nanoscale, or as an optical sensor, or as a switch.

- Also, this thesis work presents an important educational example that is worth of including into laboratory assignments for advanced physics courses. Just to mention, a simpler version of the trial function for the same problem (after Krishna Rajagopal) is included in the second edition of the Introductory Quantum Mechanics textbook by D.J.Griffith (Pearson, 2005). My trial function that has been developed in this thesis, has an advantage over Rajagopal's since it is specifically designed

to minimize and simplify the roof-line system, and so it may serve as a pedagogical example for the critical development of textbook material for students.

Appendix A. General approach to roof lines

The mechanism of roof-line integration is the following: we find *all the existing lines*, where the wave function exhibits $C_{2\mathcal{D}}^0$-type behavior, which means that the function is obviously continuous, but the first derivative has a finite discontinuity (Heaviside step). Consequently, the second derivative across the roof line represents a δ-function, thus must be taken into account in the integration.

We consider a generic function in the form of

$$F(x) = f(x)\mathrm{e}^{-\gamma g(x)} \tag{4.1}$$

and take its second derivative, yeilding

$$F''(x) = \left[f''(x) - 2\gamma f'(x)g'(x) + f(x)\left(\gamma^2 \left(g'(x)\right)^2 - \gamma g''(x) \right) \right] \mathrm{e}^{-\gamma g(x)} \tag{4.2}$$

The most general idea is to find and use only the terms, which could potentially give a δ function and will contribute to infinitesimally small x-integral $\int\limits_{a-\epsilon}^{a+\epsilon} \cdot$.

Let us now consider Rajagopal wave function in the vicinity of the line where the *exponential decay begins*. This is the only relevant roof line in our
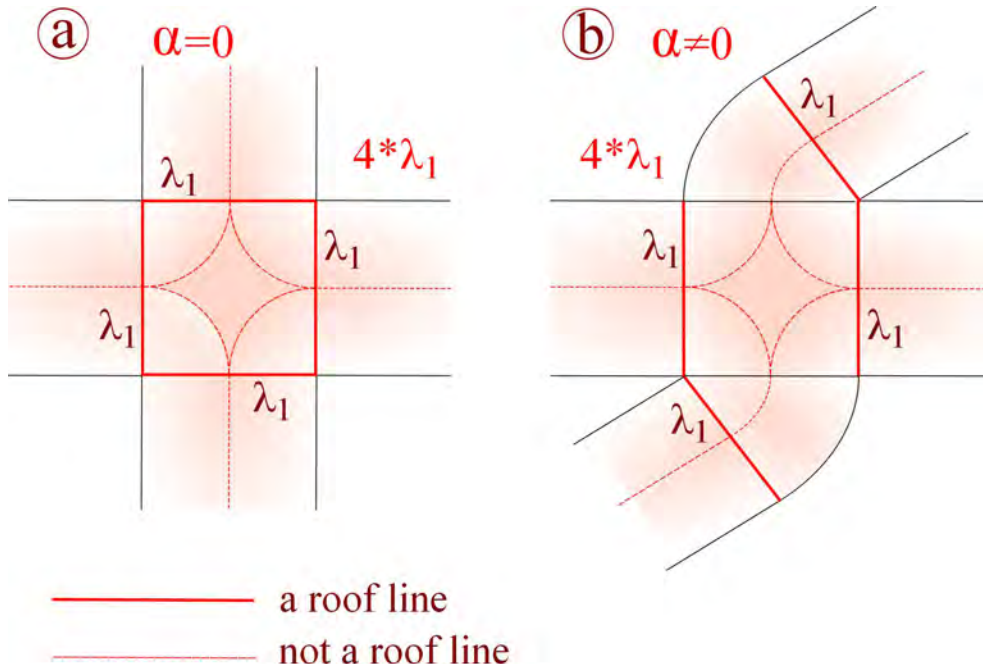
Figure 4.1: (Color online). Roof line schematics.

case. For Ψ^{Rj} we have:

$$f(x) = 1 - \frac{y}{a}\left[\theta(x-a) + \frac{x}{a}\theta(a-x)\right] \ , \tag{4.3}$$

$$g(x) = \theta(a-x) + \frac{x}{a}\theta(x-a)$$

with the second derivatives:

$$f(x)'' = \frac{y}{a^2}\delta(x-a) \ , \tag{4.4}$$

$$g(x)'' = \frac{1}{a}\delta(x-a) \ ,$$

We collect only terms containing second derivatives of $f(x)$ and $g(x)$:

$$\frac{\partial^2 \Psi_b(x,y)}{\partial x^2}\Big|_{x\to a} = (f''(x) - \gamma f(x)g'')\, \mathsf{e}^{-\gamma} = -\frac{1}{a}\delta(x-a)\left[\gamma\left(1 - \frac{y}{a}\right) - \frac{y}{a}\right]\mathsf{e}^{-\gamma}$$

The result is equivalent to that of the "canonical" solutions, provided in the textbooks. Obviously, f and g are functions of both spatial variables

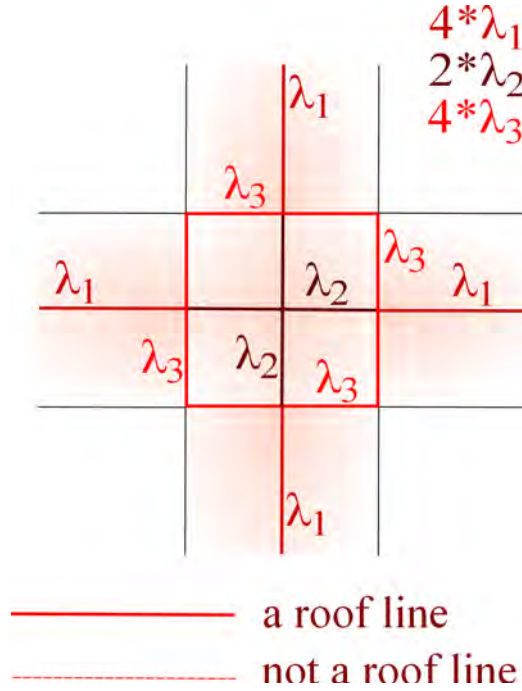$\{x, y\}$, however at this derivation we were particularly interested in the $x-$dependence.

Figure 4.2: (Color online). Roof line schematics.

For our wave function the only relevant term is:

$$-\gamma f(x) g''(x) \mathrm{e}^{-\gamma f(x)} \tag{4.5}$$

$$g''(x) = \frac{1}{a} \delta(x - a) \tag{4.6}$$

$$f(x \to a, y) = \mathcal{N} \left[1 - \left(\frac{y}{a} \right)^2 \right] \tag{4.7}$$

$$\frac{\partial^2 \Psi_b(x \to a, y)}{\partial x^2} = -\mathcal{N} \frac{\gamma}{a} \left[1 - \left(\frac{y}{a} \right)^2 \right] \delta(x - a) \mathrm{e}^{-\gamma}, \tag{4.8}$$

which confirms our results.

Bibliography

[1] Schult, R. L. and Ravenhall, D. G. and Wyld, H. W., Phys. Rev. B, 39, 8, 5476-5479 (1989); DOI: 10.1103/PhysRevB.39.5476.

[2] D. J. Griffiths, Introduction to Quantum Mechanics, 2nd ed. (Pearson Prentice-Hall, Upper Saddle River, 2005).

[3] Ledentsov, N. N., et al. "Quantum dot heterostructures: Fabrication, properties, lasers (Review)." Semiconductors 32.4 (1998): 343-365.

[4] Petroff, Pierre M., Axel Lorke, and Atac Imamoglu. "Epitaxially self-assembled quantum dots." Physics Today 54.5 (2001): 46-52.

[5] Jamieson, Timothy, et al. "Biological applications of quantum dots." Biomaterials 28.31 (2007): 4717-4732.

[6] Osika, E. N., B. Szafran, and M. P. Nowak. "Simulations of electric-dipole spin resonance for spin-orbit coupled quantum dots in the Overhauser field: Fractional resonances and selection rules." Physical Review B 88.16 (2013): 165302.

[7] Loss, Daniel, and David P. DiVincenzo. "Quantum computation with quantum dots." Physical Review A 57.1 (1998): 120.

[8] Nozik, Arthur J., et al. "Semiconductor quantum dots and quantum dot arrays and applications of multiple exciton generation to third-generation photovoltaic solar cells." Chemical reviews 110.11 (2010): 6873-6890.

[9] Bonadeo, Nicolas H., et al. "Coherent optical control of the quantum state of a single quantum dot." Science 282.5393 (1998): 1473-1476.

[10] A.I. Ekimov, A.I., Onushchenko, A.A., JETP Lett. 34 (1981) 345349.

[11] Efros, A., Efros, L., Soviet Phys. SemiconductorsUSSR 16 (1982) 772775.

[12] Brus, L. E. "A simple model for the ionization potential, electron affinity, and aqueous redox potentials of small semiconductor crystallites." The Journal of chemical physics 79.11 (1983): 5566-5571, APA.

[13] Gammon, Daniel, and Duncan G. Steel. Optical studies of single quantum dots. NAVAL RESEARCH LAB WASHINGTON DC, 2002.

[14] Reed, M. A. and Randall, J. N. and Aggarwal, R. J. and Matyi, R. J. and Moore, T. M. and Wetsel, A. E., Phys. Rev. Lett., 60, 6, 535-537 (1988).

[15] Leonard, D., et al. "Direct formation of quantum?sized dots from uniform coherent islands of InGaAs on GaAs surfaces." Applied Physics Letters 63.23 (1993): 3203-3205.

[16] P. Guyot-Sionnest C. R. Physique 9 (2008) 777787

[17] Delerue, M., Lannoo. A., Springer. p.47, (2004).

[18] M. L. Roukes, A. Scherer, S. J. Allen, Jr., H. G. Craighead, R. M. Ruthen, E.D.Beebe,and J.P.Harbison, Phys.Rev.Lett, 59, 26 (1987).

[19] G. Timp, H. U. Baranger, P. deVegvar, J. E. Cunningham, R. E. Howard, R. Behringer, and P. M. Mankiewich, Phys.Rev.Lett, 60, 20 (1987).

[20] Harold U. Baranger, A. Douglas Stone, David P. DiVincenzo, Phys.Rev.B: RC, 37, 11 (1988).

[21] Exner, P., et al. "Bound states and scattering in quantum waveguides coupled laterally through a boundary window." Journal of Mathematical Physics 37.10 (1996): 4867-4887.

[22] A.L. Delitsyn, B.T. Nguyen, and D.S. Grebenkov, Eur. Phys. J. B (2012) 85: 176.

[23] J. Goldstone, R. L. Jaffe, Phys. Rev. B, 45, 24 (1992).

[24] V. Kostrykin, ArXiv:math-ph/9806013, v.2, 15, (1999).

[25] Londergan, J. T., and D. P. Murdock. "Confined modes in two-dimensional tubes." American Journal of Physics 80.12 (2012): 1085-1093.

[26] Ernest S. Abers, *Quantum Mechanics*, University of California, Los Angeles, 2004.

[27] J. P. Carini, J. T. Londergan, D. P. Murdock, D. Trinkle, and C. S. Yung, Phys. Rev. B 55, 9842 (1997).

[28] M. L. Roukes, A. Scherer, S. J. Allen, H. G. Craighead, R. M. Ruthen, E. D. Beebe, and J. P. Harbison, Phys. Rev. Lett.59, 3011 (1987).

[29] G. Timp, H. U. Baranger, P. deVegvar, J. E. Cunningham, R. E. Howard, R. Behringer, and P. M. Mankiewich, Phys.Rev. Lett. 60, 2081 (1988).

[30] F. M. Peeters, Phys. Rev. Lett. 61, 589 (1988).

[31] F. M. Peeters, Superlattices and Microstructures 6, 217 (1989), ISSN 0749-6036.

[32] H. U. Baranger, A. D. Stone, and D. P. DiVincenzo, Phys. Rev. B 37, 6521 (1988).

[33] M. A. Reed, Sci. Am. 268, 118 (1993).

[34] F. Lenz, J. Londergan, E. Moniz, R. Rosenfelder, M. Stingl, and K. Yazaki, Annals of Physics 170, 65 (1986), ISSN 0003-4916.

[35] J. Goldstone and R. L. Jaffe, Phys. Rev. B 45, 14100 (1992).

[36] G. Dunne and R. Jaffe, Annals of Physics 223, 180 (1993), ISSN 0003-4916.

[37] P. Exner and P. Seba, Journal of Mathematical Physics 30, 2574 (1989).

[38] P. Exner, Physics Letters A 141, 213 (1989).

[39] W. H. Press, B. P. Flannery, S. A. Teukolsky, and W. T. Vetterling, Numerical recipes (Cambridge Univ. Press, 1986).

[40] F. Sols, M. Macucci, U. Ravaioli, and K. Hess, Applied Physics Letters 54, 350 (1989).

[41] J. P. Carini, J. T. Londergan, K. Mullen, and D. P. Murdock, Phys. Rev. B 46, 15538 (1992).

[42] J. P. Carini, J. T. Londergan, K. Mullen, and D. P. Murdock, Phys. Rev. B 48, 4503 (1993).

[43] C.-K. Wang, Semiconductor Science and Technology 10, 1131 (1995).

[44] L. Lewin, Theory of Waveguides (Newnes-Butterworth, London, 1975).

[45] F. Sols and M. Macucci, Phys. Rev. B 41, 11887 (1990).

[46] J. C. Wu, M. N. Wybourne, W. Yindeepol, A. Weisshaar, and S. M. Goodnick, Applied Physics Letters 59, 102 (1991).

[47] W. Yindeepol, A. Chin, A. Weisshaar, S. Goodnick, J. Wu, and M. Wybourne, in Nanostructures and Mesoscopic Systems,edited by W. P. Kirk and M. A. Reed (Academic Press, Boston, 1992), pp. 139149, ISBN 978-0-12-409660-8.

[48] C.-K. Wang, K.-F. Berggren, and Z.-L. Ji, Journal of Applied Physics 77, 2564 (1995)

[49] S. Nepal, L Zhemchuzhna, A Meliksetyan and I.V.Bondarev, Bound electron states in skew-symmetric quantum wire intersections, Bulletin of the American Physical society, **59**, H1.00149 (2014).